UNIVERSIDADE FEDERAL DO RIO GRANDE DO SUL
INSTITUTO DE FÍSICA
DEPARTAMENTO DE ASTRONOMIA

A natureza dos braços espirais nucleares na galáxia ativa Arp 102B

Guilherme dos Santos Couto

Dissertação realizada sob orientação da Professora Dra. Thaisa Storchi-Bergmann e apresentada ao Programa de Pós-Graduação do Instituto de Física da UFRGS em preenchimento parcial dos requisitos para a obtenção do título de Mestre em Física.

Porto Alegre, RS, Brasil
5 de Novembro de 2012

Agradecimentos

Agradeço aos meus pais, de onde sempre tirei todo apoio para poder seguir fazendo o que gosto, por sempre me aconselharem sabiamente sobre os caminhos da vida, que pouco sei, e principalmente pelo amor incondicional. À minha irmã, pela amizade única que poucas pessoas são providas, onde se conhece o outro como a si mesmo. Agradeço à minha família toda, sem exceção, pelas horas de diversão e carinho mais valiosas que terei na vida.

Agradeço à todos meus colegas de departamento e grupo de pesquisa, pelo infindável conhecimento e suporte acadêmico, pelo estimulante ambiente de partilha da ciência, pelo acolhimento e carinho. À Thaisa, em quem me espelho na busca de ser um pesquisador melhor, e por acreditar no meu trabalho.

Agradeço aos meus amigos da vida, em especial os mais íntimos, que, mesmo depois de tanto tempo de vivência, ansio cada encontro como se fosse o último. Muito obrigado por confiar em mim uma amizade tão especial.

À ciência, o centro de tudo, o que me motiva a saber mais, mesmo que no caminho descubra que sei menos, num círculo vicioso apaixonante.

À Natacha, da onde tirei a força durante todo esse trabalho, sem a qual não teria a alegria e o apoio necessário.

Guilherme dos Santos Couto

Universidade Federal do Rio Grande do Sul
5 de Novembro de 2012

Resumo

Neste trabalho estudamos a região central da galáxia LINER/Seyfert 1 Arp 102B na tentativa de descobrir a natureza dos recentemente descobertos braços espirais nucleares. Apresentamos uma análise bi-dimensional da excitação e cinemática do gás nos 2.5 kpc× 1.7 kpc internos, a partir de espectros ópticos obtidos com o espectrógrafo de campo integral do instrumento GMOS no telescópio Gemini Norte, com resolução espacial de $\approx$ 250 pc. Nossos mapas de fluxo nas linhas de emissão mostram os mesmos braços espirais nucleares descobertos em imagens feitas com o Telescópio Espacial Hubble. Um jato rádio, observado em 8.4 GHz com o VLA, está correlacionado com o braço espiral a leste. Outro braço é observado a oeste. Valores de razões de linhas típicos de núcleos ativos excluem ionização do gás por estrelas, restando choques e radiação diluída como possíveis fontes de ionização. Uma região de alta densidade do gás é observada na borda ao norte do braço leste, numa região onde o jato rádio parece ser deflexionado. Mapas de velocidade centróide mostram um padrão de rotação distorcido, com *blueshifts* a leste e *redshifts* a oeste. *Channel maps* mostram *blueshifts* e *redshifts* no local do jato rádio (e braço a leste), sendo interpretados como originados na parede de frente e de trás de um outflow empurrado pelo jato rádio, que é lançado perto do plano do céu. Um disco em rotação é bem ajustado no mapa de velocidade centróide, exceto numa região de possível *outflow*, a sudeste do núcleo, mesma região onde se observa uma alta dispersão de velocidade. Estimamos uma taxa de *outflow* de $0.8 - 3.8 \times 10^{-2}\,\mathrm{M_\odot\,yr^{-1}}$, um pouco maior que a taxa de acreção ao núcleo ativo. Propomos um cenário em que o gás foi recentemente capturado por Arp 102B numa interação com Arp 102A, num disco inclinado e desencadeando a atividade nuclear. Um jato nuclear é lançado perto do plano do céu e da linha dos nodos, empurrando o gás circumnuclear e dando origem aos braços espirais.

Abstract

In this work we studied the LINER/Seyfert 1 galaxy Arp 102B in order to unveil the nature of its newly discovered nuclear spiral arms. We present a two-dimensional analysis of the gaseous excitation and kinematics of the inner 2.5 kpc$\times$ 1.7 kpc, from optical spectra obtained with the GMOS integral field spectrograph on the Gemini North telescope at a spatial resolution of $\approx$ 250 pc. Our GMOS-IFU emission-line maps display the same two-armed nuclear spiral as previously observed with the HST-ACS camera. A 8.4 GHz VLA bent radio jet correlates with the east spiral arm. Another arm is seen to the west. Emission line ratios typical of active nuclei rule out ionization by stars, leaving shocks and diluted radiation as possible ionizing sources for the gas. A knot of high gas density is observed in the northern border of the east arm, at a region where the radio jet seems to be deflected. Centroid velocity maps display a distorted rotation pattern, with blueshifts to the east and redshifts to the west. Lower blueshifts are shown along the radio jet. Channel maps show blueshifts and redshifts at the jet location (and eastern arm), being interpreted as originated in the front and back walls of an outflow pushed by the radio jet, which is launched close to the plane of the sky. The gas kinematics is well reproduced by a rotating disk except in a possible outflow region, south-east from the nucleus, where the gas shows high velocity dispersion. We estimate a mass outflow rate in the range $0.8 - 3.8 \times 10^{-2}\,\mathrm{M_\odot\,yr^{-1}}$, which is just somewhat higher than the mass accretion rate to the active nucleus. We propose a scenario in which gas has been recently captured by Arp 102B in an interaction with Arp 102A, settling in an inclined disk rotating around the nucleus of Arp 102B and triggering its nuclear activity. A nuclear jet is launched close to the plane of the sky and the line of nodes, pushing the circumnuclear gas and giving origin to the nuclear arms. The knot of high velocity residuals can be interpreted as another (more compact) outflow, with a possible counterpart to the north-west.

Conteúdo

Lista de Figuras

Abreviaturas

ACS: De *Advanced Camera for Surveys*. Câmera do Telescópio Espacial Hubble.
AGN: Núcleo ativo de galáxias (*Active Galactic Nuclei*).
BLR: Região de linhas largas (*Broad-Line Region*).
ESO: Observatório Europeu do Sul (*European Southern Observatory*).
EVN: De *European VLBI Network*, consórcio europeu do VLBI.
FOV: Campo de visão (de *Field-of-View*).
FR-I e FR-II: Classificações de Fanaroff-Riley tipo I e II, respectivamente.
FWHM: Largura a meia altura (de *Full Width at Half Maximum*).
GMOS: Espectrógrafo do telescópio Gemini (de *Gemini Multi-Object Spectrograph*).
HST: Telescópio Espacial Hubble (*Hubble Spacial Telescope*).
IDL: Linguagem de programação, de *Interactive Data Language*.
IFU: Unidade de campo integral (de *Integral Field Unit*).
LINER: Núcleo com emissão de linhas de baixa ionização (de *Low-Ionization Nuclear Emission-line Region*).
NASA: Agência espacial americana (de *National Aeronautics and Space Administration*).
NLR: Região de linhas estreitas (de *Narrow Line Region*).
NRAO: Observatório americano de radioastronomia (de *National Radio Astronomy Observatory*).
PCA: Análise de componentes principais (de *Principal Component Analysis*).
SDSS: De *Sloan Digital Sky Survey*, survey de imageamento e espectroscopia.
SMBH: Buraco negro supermassivo (de *Supermassive Black Holes*).
STIS: Espectrógrafo do Telescópio Espacial Hubble (de *Space Telescope Imaging Spectrograph*).
VLA: De *Very Large Array*, observatório radioastronômico.
VLBI: De *Very Long Baseline Interferometry*, interferômetro radioastronômico.

Capítulo 1

Introdução

Evidências observacionais acumuladas principalmente depois do lançamento do Telescópio Espacial Hubble indicam que todas as galáxias que tem um bojo estelar hospedam buracos negros supermassivos (SMBHs, de *supermassive black holes*) em seus centros (Ferrarese & Merritt, 2000, Gebhardt et al., 2000). Chamamos de galáxias ativas aquelas onde a região central emite radiação que não pode ser reproduzida somente pela superposição de espectros estelares, ou seja, a radiação é de origem não-estelar, e é emitida em todos os intervalos do espectro eletromagnético. Os menos luminosos ($L < 10^{42}\,\mathrm{erg\,s^{-1}}$) são os LINERs (de *low-ionization nuclear emission-line region*) e os mais luminosos ($L > 10^{42}\,\mathrm{erg\,s^{-1}}$) são os Quasares. Na faixa de rádio frequência, a radiação emitida por alguns núcleos de galáxias ativas (AGNs, de *active galactic nucleus*) é de natureza sincrotrônica (ou seja, gerada quando partículas carregadas são aceleradas radialmente), como é o caso das rádio-galáxias. No caso específico das rádio-galáxias, são também atribuídos a AGNs a formação de jatos relativísticos originados dos fortes campos magnéticos gerados próximo ao SMBH, além de variabilidade na emissão espectral.

Por serem muitas vezes objetos muito luminosos, podem ser observados a grandes distâncias, possibilitando o estudo de evolução de galáxias, e também servem como parâmetros em modelos cosmológicos. O estudo da física desses objetos é fundamental para podermos entender a formação das galáxias atuais.

1.1 AGNs e Galáxias Ativas

A atividade nuclear é a manifestação dos processos físicos que ocorrem em torno do SMBH central, que tem massas entre 10^6 e 10^{10} $\mathrm{M_\odot}$ (Ferrarese & Ford, 2005, McConnell et al., 2011). O SMBH é delimitado pelo raio de Schwarschild, que pode

ser calculado através da equação

$$R_{Sch} = \frac{2GM_\bullet}{c^2} \tag{1.1}$$

onde $M_\bullet$ é a massa do SMBH, G é a constante gravitacional e c é a velocidade da luz no vácuo. O raio de Schwarschild delimita o horizonte de eventos do SMBH, região em que a força gravitacional é tão forte que nem mesmo a luz é capaz de escapar, fazendo com que eventos interiores não sejam percebidos por observadores exteriores. Para SMBHs com massas entre 10^6 e 10^{10} $M_\odot$, o raio de Schwarschild varia de $10^{-7} \lesssim R_{Sch} \lesssim 10^{-2}$ pc.

Segundo modelos unificados de AGN (Antonucci, 1993, Urry & Padovani, 1995) o SMBH é envolvido por um disco de acreção formado por gás aquecido por dissipação de energia na transferência de matéria das partes externas do disco até o SMBH. Energia cinética, térmica e radiativa é gerada a partir da energia potencial gravitacional da massa capturada. Sendo aquecido a altas temperaturas, o gás emite em todos os comprimentos de onda, com um excesso no ultravioleta. A emissão do disco de acreção ioniza o gás externo, que por sua vez emite radiação não-térmica. O disco de acreção tem dimensão comparável ao sistema solar. Dependendo da massa do SMBH, o disco de acreção pode ter diâmetro entre 10^{-4} a 10^{-1} pc (Morgan et al., 2010).

Além do disco de acreção temos mais para fora a região de linhas largas (BLR, de *broad-line region*), formada por gás com altas velocidades orbitais, em torno de $5000\,\mathrm{km\,s^{-1}}$. H$\alpha$ $\lambda6563\,\mathring{A}$ e Hβ $\lambda4861\,\mathring{A}$ são dois exemplos de linhas de emissão largas usualmente observadas em espectros no óptico de AGNs. A largura das linhas é devida à dispersão de velocidades do gás emissor, que deve seu movimento orbital ao forte potencial gravitacional do SMBH. As nuvens localizadas nessa região são excitadas pela radiação vinda do disco de acreção. A análise das linhas largas dá informações sobre a cinemática mais interna do AGN. Nem o disco de acreção nem a BLR são resolvidos espacialmente por telescópios atuais, sendo possível identificá-los apenas por métodos indiretos, como mapeamento por reverberação (Peterson et al., 2004).

Um toro de gás molecular se localiza em torno da BLR fazendo com que a visão do núcleo seja bloqueada em determinados ângulos de visão. Seu raio interno é definido pela região mais próxima do disco de acreção, onde a poeira é capaz de sobreviver à radiação ionizante. Logo o raio depende da luminosidade intríseca do disco de acreção. Suas dimensões ficam entre 1 e 100 pc (Elitzur, 2006). No caso de impedimento da visualização da BLR, o AGN é classificado como tipo 2, caso

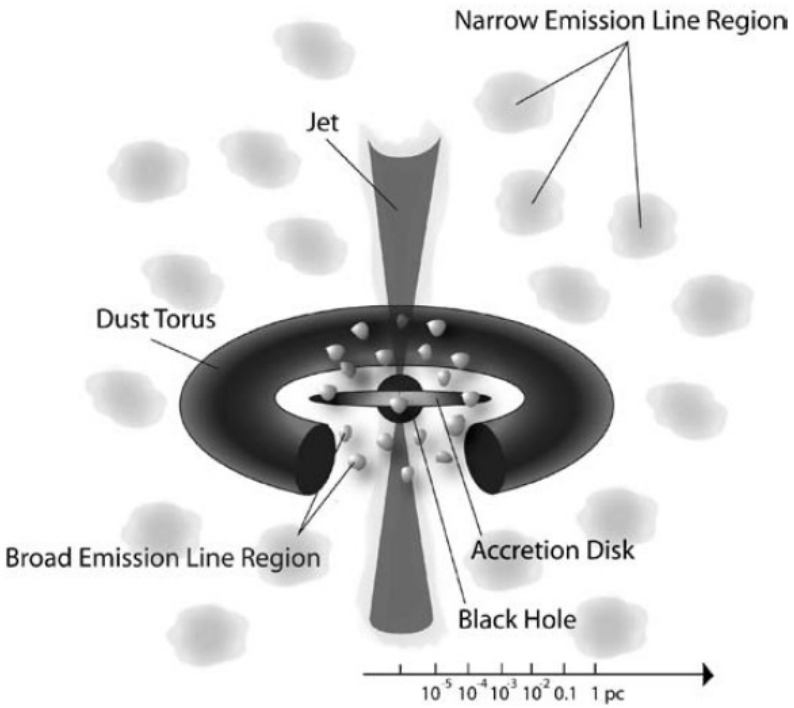

Figura 1.1: Ilustração do modelo unificado de AGNs. As principais estruturas estão representadas, assim como suas escalas. Da região central à parte mais externa observamos: o SMBH, disco de acreção, região de linhas largas, toróide de poeira, região de linhas estreitas e jatos relativísticos. Figura retirada de Ferrarese & Ford (2005).

contrário ele é do tipo 1. Na Fig. 1.1 está ilustrado um dos modelos unificados mais utilizados.

A região de linhas estreitas (NLR, de *narrow-line region*) fica além da BLR, tem dimensões de centenas de pc até unidades de kpc, e é formada por gás com dispersão de velocidades menores, em torno de centenas de $\mathrm{km\,s^{-1}}$. A emissão de linhas estreitas no espectro por essa região resulta da velocidade mais baixa se comparada à BLR, já que o gás está mais distante do centro do potencial gravitacional. A baixa densidade do gás (em torno de $10^3\,\mathrm{cm^{-3}}$) faz com que o gás, excitado colisionalmente, seja desexcitado radiativamente, gerando emissão em linhas proibidas, como [O III] $\lambda\,5007$ e [S II] $\lambda\,6731$. Por estar localizada numa escala espacial maior que a BLR, é possível resolver essa região com os telescópios atuais. Assim podemos analisar a cinemática espacialmente, inclusive estudar os mecanismos de ejeção de gás.

Em muitos AGNs ocorre a presença de jatos relativísticos. Esses jatos, na maioria das vezes perpendiculares ao disco de acreção, são formados por parte da matéria acretada pelo disco, que é acelerada relativísticamente, possivelmente devido ao

campo magnético do AGN. Jatos relativísticos podem chegar a centenas de kiloparsecs, podendo influenciar a morfologia e evolução da galáxia hospedeira.

1.2 Rádio-Galáxias e outras classificações de AGNs

Rádio-Galáxias são um tipo de galáxia ativa caracterizadas por sua alta luminosidade (de 10^{28} a 10^{36} erg seg^{-1} Hz^{-1}) em comprimentos de onda de rádio (usualmente medido em 1.5 GHz). Foram descobertas e mapeadas na década de 50. Normalmente apresentam nesta faixa de frequência, uma fonte nuclear em escalas de subparsecs, além de jatos e geralmente um par de lóbulos gigantes (como visto em Centaurus A, Fig. 1.2). Suas regiões emissoras de rádio podem se estender a distâncias maiores que o raio da própria galáxia hospedeira. As diferentes formas dos lóbulos fez com que se introduzisse uma nova classificação dentro das rádio galáxias: Fanaroff-Riley tipo I e II (Fanaroff & Riley, 1974), onde a diferença de um tipo para o outro é a razão entre: a distância entre o núcleo e o ponto mais brilhante do jato e o comprimento total do jato. FRs tipo I tem razão menor que 0.5 e de tipo II maior que 0.5 (Fig. 1.3). Essa classificação está intimamente ligada à luminosidade total em rádio. FRs tipo I tem luminosidade em 178 MHz abaixo de $2 \times 10^{25}\,\mathrm{W\,Hz^{-1}\,srt^{-1}}$, enquanto galáxias de tipo II excedem esta luminosidade. Outra característica das rádio-galáxias é que a maioria das galáxias hospedeiras são do tipo elípticas.

Como mencionado anteriormente, há ainda outras classes de galáxias ativas, dependendo da luminosidade e do tipo espectral. Quasares são muito luminosos em todos os comprimentos de onda tendo uma luminosidade tão alta que podem ser observados às maiores distâncias no universo. Já LINERs são núcleos ativos em geral pouco luminosos definidos pela razão entre suas linhas espectrais (Heckman, 1980). O espectro típico de LINER possui emissão mais intensa de linhas de baixa ionização, como o [O I] $\lambda\,6300$ e [N II] $\lambda\,6548$, quando comparado com as linhas de alta ionização, que são de menor intensidade.

Galáxias Seyfert possuem em geral baixa emissão em rádio. Possuem espectro similar ao de quasares, mas são menos luminosos que estes. Logo, podemos identificar com facilidade a galáxia hospedeira, algo que não ocorre com quasares. Seyferts emitem fortemente em linhas de alta ionização e são classificadas como de tipo 1, quando possuem emissão em linhas largas, ou de tipo 2, quando não possuem.

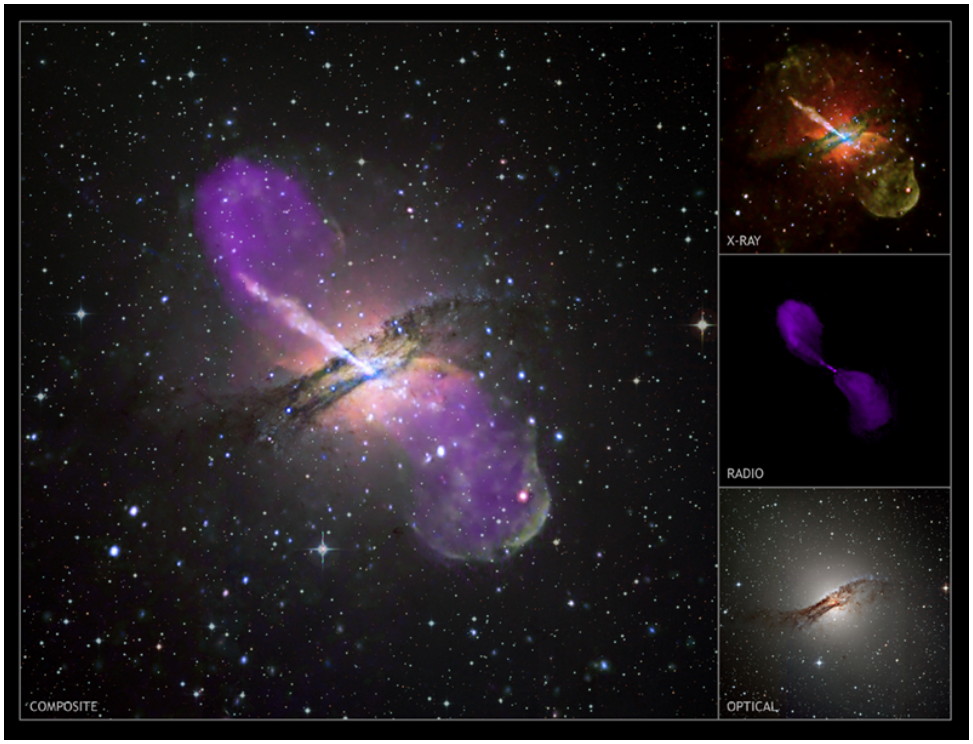

Figura 1.2: Centaurus A, a rádio-galáxia mais próxima, em um mosaico de observações em raio-X, rádio e óptico. Créditos: NASA e ESO.

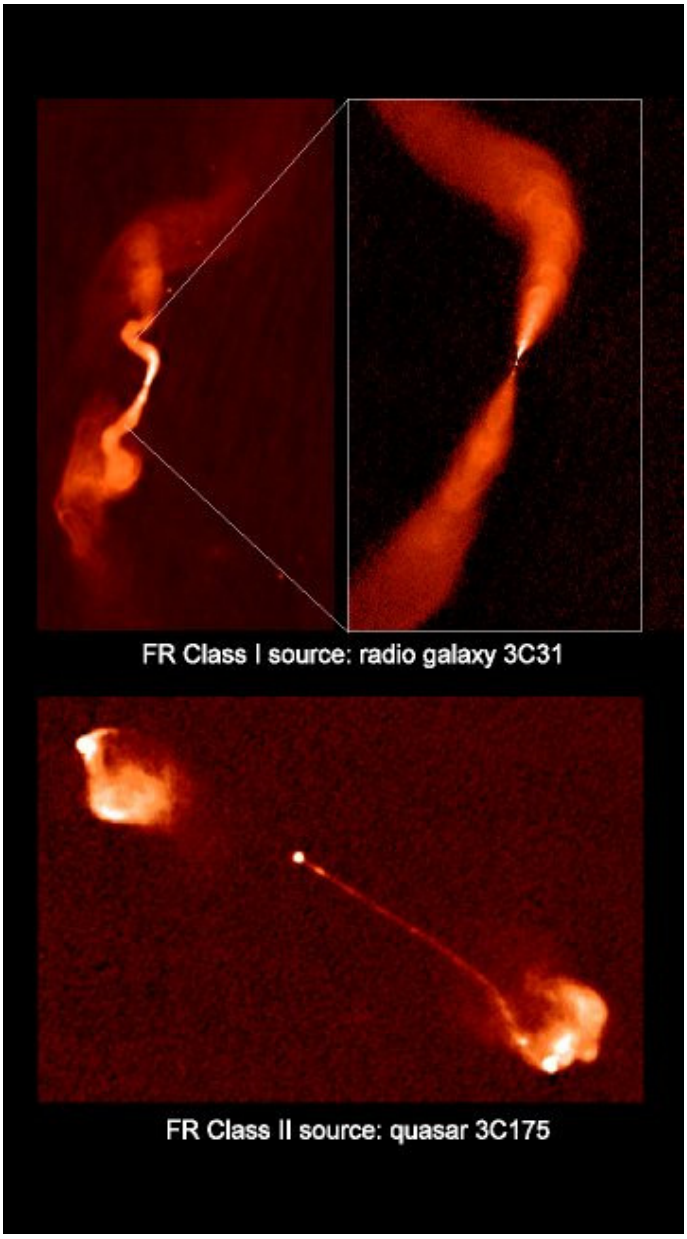

Figura 1.3: Acima a galáxia 3C31 (classificada com FR-I) e abaixo a galáxia 3C175 (classificada como FR-II). Os jatos em rádio chegam a distâncias muitas vezes maiores que a extensão da galáxia. Créditos: NRAO.

1.3 Braços espirais nucleares

Evidências recentes tem apontado que braços espirais nucleares, formados dentro dos kiloparsecs centrais das galáxias, são ricos em poeira e gás e são comuns em AGNs (Martini et al., 2003, Simões Lopes et al., 2007). Essas espirais compactas tem sido sugeridas como um mecanismo possível para trazer gás das partes externas ao centro da galáxia e servir de combustível para o SMBH (Maciejewski, 2004). Fathi et al. (2006) de fato mapearam movimentos de gás ionizado em direção ao centro da galáxia LINER NGC 1097 ao longo das espirais nucleares (também encontrado em Prieto et al., 2005, Davies et al., 2009), e Storchi-Bergmann et al. (2007) acharam movimentos similares na espiral nuclear que circunda outro núcleo de galáxia LINER, a NGC 6951. Outros casos similares também foram encontrados na Seyfert 1 NGC4051 (Riffel et al., 2008), na LINER/Seyfert 1 M81 (Schnorr Müller et al., 2011) e na Seyfert 2 Mkr 1066 (Riffel et al., 2010), apenas para citar alguns exemplos.

A maioria dos braços espirais nucleares não são associados a formação estelar e mostram contrastes baixos de densidade, diferentemente dos braços espirais maiores nos discos das galáxias. As estruturas de poeira desses braços parecem ser assinaturas de frentes de ondas de choque sendo propagadas num gás circumnuclear não auto-gravitante (Martini & Pogge, 1999).

1.4 A galáxia Arp 102B

A galáxia Arp 102B é uma rádio-galáxia com linhas de emissão de Balmer muito largas (correspondete a dispersão de velocidades de $\approx 10.000\,\mathrm{km\,s^{-1}}$) e com duplo-pico, e um espectro óptico de linhas estreitas do tipo LINER (Chen et al., 1989, Chen & Halpern, 1989), levando a uma classificação de LINER/Seyfert 1. Chen et al. (1989) e Chen & Halpern (1989) modelaram a emissão de duplo-pico como originária da parte externa do disco de acreção em rotação Kepleriana, iluminada e ionizada por um *torus* iônico quente localizado na parte interna do disco de acreção. Linhas de emissão de duplo-pico largas foram achadas em outros núcleos de galáxias ativas (AGNs), incluindo outras rádio-galáxias como a 3C 390.3 (Oke, 1987, Perez et al., 1988) e LINERs como a NGC 1097 (Storchi-Bergmann et al., 1993, 2003), com a Arp 102B sendo considerada a "prototípica emissora de duplo-pico".

Apesar de Arp 102B ser classificada como uma galáxia E0, foram encontrados (Fathi et al., 2011) braços espirais compactos em imagens feitas no contínuo (6000 $\AA$)

Figura 1.4: Par de galáxias Arp 102A e Arp 102B. A orientação é a mesma que das observações com o IFU (ver capítulo 2), com um ângulo de 65° entre o norte e o eixo vertical da imagem, estando o norte norte à direita. Arp 102B é a galáxia elíptica no canto inferior esquerdo da imagem. Créditos: Rick Johnson. A imagem original feita pelo astrônomo pode ser vista em *http://www.spacebanter.com/attachment.php?attachmentid=4120&stc=1.*

e num filtro de banda estreita que isola a emissão na linha Hα obtidas com a *Advanced Camera for Surveys* (ACS) do *Hubble Space Telescope* (HST). Foi especulado que a origem dos braços nucleares seja a interação com a galáxia companheira Arp 102A (Stauffer et al., 1983, ver imagem das duas galáxias na Fig. 1.4). Esta interação pode estar provocando uma queda do gás ao centro de Arp 102B alimentando o SMBH e desencadeando a atividade nuclear observada. Todavia, em Fathi et al. (2011), foi encontrada uma correlação espacial do braço espiral a leste (o outro está direcionado a oeste) com um jato rádio curvo, sem jato oposto. Esta correlação sugere que o braço espiral pode ser o resultado de uma interação do jato rádio com o gás circumnuclear da galáxia.

Nós adotamos uma distância de 104.9 Mpc a Arp 102B, o que resulta numa escala de 490.2 pc arcsec^{-1} na galáxia (Eracleous & Halpern, 2004).

1.5 O jato rádio da galáxia Arp 102B

A primeira detecção da emissão em rádio foi feita por Biermann et al. (1981), utilizando dados do VLBI (de *Very Long Baseline Interferometry*) em 5 GHz. Neste trabalho a classificação Seyfert 1 foi proposta devido a sua intensa emissão em raios-X ($1 \times 10^{43} \mathrm{ergs\,s^{-1}}$ na banda de $0.5 - 4.5$ keV), obtida na literatura, quando comparada com o óptico. Emissão estendida em rádio num jato único (somente para um lado), contribuindo com aproximadamente 30% da emissão total, foi encontrada por Puschell et al. (1986) a partir de dados do VLA (de *Very Large Array*) em 4.9 GHz. Porém, não puderam determinar o mecanismo de emissão da radiação. A possibilidade de projeção dos lóbulos na direção da linha de visada foi levantada, mas concluiu-se que a emissão estendida é muito mais fraca do que nas extensões típicas de rádio galáxias.

Caccianiga et al. (2001), estudando o par Arp 102A e Arp 102B com dados do EVN (*European VLBI Network*) em 5 GHz, demonstraram que a alta temperatura de brilho da emissão rádio ($> 10^8$ K) é muito alta para que o mecanismo de produção seja térmico (como produzido por uma taxa de formação estelar alta), cujas temperaturas esperadas são de no máximo 10^5 K. Sendo assim, esses autores vincularam a emissão em rádio a um jato relativístico. Fathi et al. (2011) propusera que a velocidade do jato é de $\approx 0.45c$, considerando-o perpedincular ao disco de acreção, modelado por Chen & Halpern (1989) com ângulo de inclinação de 33°. A assimetria do jato foi vinculada ao Doppler *boosting* [1] gerado por emissão na direção da linha de visada.

Embora os jatos rádio sejam na sua maioria bi-polares, Arp 102B não é o primeiro caso de jato observado somente para um lado. Wrobel et al. (1988), por exemplo, estudaram o jato rádio da galáxia elíptica NGC 6146, mas não conseguiram determinar se o fato do jato ter apenas um lado é devido a um boosting relativístico sofrido pelo lado próximo ou se um lado é mais potente que o outro. Ainda foi levantada a hipótese de ser apenas uma fonte emissora de rádio com uma extremidade, descartando a classificação de jato, mas isso não foi favorecido, já que a emissão era muito menos estendida (≈ 1 kpc) do que a esperada nesses casos (dezenas de kpcs). Kovalev et al. (2007) estudaram a rádio galaxia M87, que apresenta uma poderosa emissão em rádio, apenas para um lado do núcleo. Os autores concluíram que modelos de *boosting* relativísticos não explicariam a morfologia do jato, e propuseram

[1] Doppler *boosting* é um efeito em que, quando ocorre uma projeção de uma fonte emissora no sentido do observador, a radiação emitida nessa direção é fortalecida, enquanto que a radiação contrária é enfraquecida.

outros cenários, como o jato ser intrinsicamente assimétrico.

1.6 Objetivos

Nossos objetivos neste estudo são investigar a natureza dos braços espirais em Arp 102B e sua relação com a alimentação do SMBH e/ou seu *feedback*. Para isto, mapeamos a excitação e a cinemática do gás nos kiloparsecs centrais de Arp 102B, analisando a possível interação entre o jato rádio e o gás emissor de linhas. Este estudo objetiva também estudar a natureza da fonte ionizante do gás emissor.

Capítulo 2

Kinematics and excitation of the nuclear spiral in the active galaxy Arp 102B

Mon. Not. R. Astron. Soc. **000**, 1–?? (2011) Printed 5 November 2012 (MN LATEX style file v2.2)

Kinematics and excitation of the nuclear spiral in the active galaxy Arp 102B

Guilherme S. Couto[1⋆], Thaisa Storchi-Bergmann[1], David J. Axon[2], Andrew Robinson[2], Preeti Kharb[2] and Rogemar A. Riffel[1,3]
[1] *Universidade Federal do Rio Grande do Sul, IF, CP 15051, Porto Alegre 91501-970, RS, Brazil*
[2] *Physics Department, Rochester Institute of Technology, 85 Lomb Memorial Dr., Rochester, NY 14623, USA*
[3] *Universidade Federal de Santa Maria, Departamento de Física, Centro de Ciências Naturais e Exatas, 97105-900, Santa Maria, RS, Brazil*

5 November 2012

ABSTRACT
We present a two-dimensional analysis of the gaseous excitation and kinematics of the inner $2.5 \times 1.7\,\mathrm{kpc}^2$ of the LINER/Seyfert 1 galaxy Arp 102B, from optical spectra obtained with the GMOS integral field spectrograph on the Gemini North telescope at a spatial resolution of $\approx$ 250 pc. Emission-line flux maps show the same two-armed nuclear spiral we have discovered in previous observations with the HST-ACS camera. One arm reaches 1 kpc to the east and the other 500 pc to the west, with a 8.4 GHz VLA bent radio jet correlating with the former. Gas excitation along the arms is low, with line ratios typical of LINERs, and which rule out gas ionization by stars. The gas density is highest ($\approx$500 - 900 cm^{-3}) at the nucleus and in the northern border of the east arm, at a region where the radio jet seems to be deflected. Centroid velocity maps suggest that most gas is in rotation in an inclined disk with line of nodes along position angle $\approx$ 88°, redshifts to the west and blueshifts to the east, with lower blueshifts correlated with the eastern arm and radio jet. This correlation suggests that the jet is interacting with gas in the disk. Channel maps show blueshifts but also some redshifts at the eastern arm and jet location which can be interpreted as originated in the front and back walls of an outflow pushed by the radio jet, suggesting also that the outflow is launched close to the plane of the sky. Principal Component Analysis applied to our data supports this interpretation. We estimate a mass outflow rate in the range $0.8 - 3.8 \times 10^{-2}\,\mathrm{M}_\odot\,\mathrm{yr}^{-1}$, which is just somewhat higher than the mass accretion rate to the active nucleus. We propose a scenario in which gas has been recently captured by Arp 102B in an interaction with Arp 102A, settling in an inclined disk rotating around the nucleus of Arp 102B and triggering its nuclear activity. A nuclear jet is pushing the circumnuclear gas, giving origin to the nuclear arms. A blueshifted emitting gas knot is observed at $\approx$ 300 pc south-east from the nucleus and can be interpreted as another (more compact) outflow, with a possible counterpart to the north-west.

Key words: Galaxies: individual Arp 102B – Galaxies: active – Galaxies: Seyfert – Galaxies: nuclei – Galaxies: kinematics – Galaxies: jets

1 INTRODUCTION

Dusty spirals have been recently discovered to be common nuclear structures (within the inner kpc) of active galaxies (Martini et al. 2003; Simões Lopes et al. 2007). These compact spirals have been suggested to be possible mechanisms to channel gas inwards to fuel the nuclear supermassive black hole (SMBH, Maciejewski 2004), with some recent observational work supporting such hypothesis (Prieto et al. 2005; Fathi et al. 2006; Storchi-Bergmann et al. 2007; Riffel et al. 2008; Davies et al. 2009; Schnorr Müller et al. 2011; Riffel & Storchi-Bergmann 2011).

Most nuclear spiral arms seem not to have associated star formation and show low density constrasts, unlike the larger spiral arms in the disks of the galaxies. The dust structures in these arms seem to be signatures of shock fronts of waves propagating in non self-gravitating circumnuclear gas (Martini & Pogge 1999).

⋆ E-mail:gcouto@if.ufrgs.br

In a previous study (Fathi et al. 2011, hereafter Paper I), we have reported the discovery of a two-armed nuclear spiral in a narrow-band Hα image of the active galaxy Arp 102B obtained with the *Hubble Space Telescope* (HST) ACS Camera. The origin of the nuclear spiral has been speculated to be the interaction with the companion galaxy Arp 102A (Stauffer, Schild & Keel 1983) and could also be tracing inflows triggered by this interaction. An image of the two galaxies[1] does indeed show a tidal arm originating in the gas rich spiral galaxy Arp102A which connects with Arp102B from the north-east. Nevertheless, in Paper I, we also found that the spiral arm to the east (the other is to the west) is spatially correlated with a bent radio jet, suggesting that the spiral could be the result of the interaction of a radio jet with circumnuclear gas at the galaxy. The first detection of radio emission was made by Biermann et al. (1981), but it was found to have a jet-like structure only later by Puschell et al. (1986). These authors were not able to determine the radio emission mechanism. Caccianiga et al. (2001), studying the pair Arp 102A and Arp 102B, demonstrated that the radio jet was originated in an AGN, rather than in a starburst, since its brightness temperature ($10^6 - 10^8$ K) is too high to be due to starburst emission, whose values are at most 10^5 K. In Paper I, we concluded that, in order to gauge the jet impact on the circumnuclear gas it would be necessary to map the gas excitation and kinematics. Such a study would also provide constraints on the nature of the ionizing source as well as on the presence of outflows and/or inflows along the spiral arms, allowing us to investigate their nature. This is the goal of the present study.

One particular characteristic of the active nucleus of Arp 102B is the presence of very broad ($\approx$10,000 kms) and double-peaked Balmer lines in its optical spectra. In fact, Arp 102B is considered to be the prototypical "double-peaker" (Chen, Halpern & Filippenko 1989; Chen & Halpern 1989; Newman et al. 1997; Flohic & Eracleous 2008). The Arp 102B nucleus is classified as a LINER/Seyfert 1 being more luminous but other than that similar to the one in NGC 1097 (Storchi-Bergmann et al. 1993, 2003; Fathi et al. 2006). Arp 102B is classified as an E0 galaxy, thus the presence of the gaseous spiral arms was unexpected. We adopt a distance to Arp 102B of 104.9 Mpc, which gives a scale of 490.2 pc arcsec^{-1} at the galaxy (Eracleous & Halpern 2004).

This paper is organized as follows: in Sec. 2 we describe the observations and data reduction, in Sec. 3 we present the results for the gas excitation and kinematics, in Sec. 4 we discuss our results and in Sec. 5 we present our conclusions.

2 OBSERVATIONS AND DATA REDUCTION

2.1 IFU Data

Two-dimensional optical spectroscopy data were obtained at the Gemini North Telescope with the *Gemini Multi-Object Spectrograph Integral Field Unit* (GMOS IFU) (Allington-Smith et al. 2002) in April 06, 2007, as part of program GN-2007A-Q-57, and comprise six individual exposures of 900 s centred at λ 5850Å with a spectral coverage from λ4400Å to λ7300Å. The B600+_G5303 grating with the IFU-R mask was used. The spectral resolution is 1.8Å at Hα ($\approx$85 km s^{-1}) – derived from the full width at half maximum (FWHM) of the CuAr lamp emission lines – and the angular resolution is 0.6 arcsec (corresponding to 245 pc at the galaxy) – adopted as the FWHM of the spatial profile of the flux calibration star, Feige 66. The GMOS IFU has a rectangular field of view, of approximately $5\farcs1 \times 3\farcs4$, corresponding to 2.5 kpc$\times$ 1.7 kpc at the galaxy. The major axis of the IFU was oriented along position angle PA=65°.

The data reduction was accomplished using tasks in the GEMINI.GMOS IRAF package as well as generic IRAF tasks. The reduction procedure included trimming of the images, bias subtraction, flat-fielding, wavelength calibration, s-distortion correction, sky subtraction and relative flux calibration. In order to obtain an absolute flux calibration, we have scaled our IFU data to long-slit data obtained with the *HST*-STIS spectrograph. This was accomplished by dividing our fluxes by 15, in order to match the fluxes obtained with STIS within the same apertures. In order to improve the spatial resolution, we have corrected the data for differential atmospheric refraction (Steiner et al. 2009) and then applied a Richardson-Lucy deconvolution algorithm (Richardson 1972; Lucy 1974) to the final datacube, which resulted in a spatial resolution of $\approx 0\farcs5$.

Table 1. *STIS observations*

Slit	PA (°)	platescale ($''$pix^{-1})	exposure time (s)
POS1	-19.9	0.05	4488.
POS2	-94.3	0.05	4450.
offcen1 (west)	-19.9	0.1	2870.
offcen2 (east)	-19.9	0.1	2874.

2.2 STIS Data

We used the *HST*-STIS spectrograph and the G750M grating centered at λ_{cen} = 6768 Å to obtain spectra of Arp 102B along two position angles: -19.9° (north-west–south-east) and -94.3° (east-west), as part of the program GO-9782 (PI: David J. Axon). The corresponding spectral range is 6482–7054Å, centered on the Hα emission line, but also including [O I]$\lambda\lambda$6300,6364, [N II]$\lambda\lambda$6548,6583, and [S II]$\lambda\lambda$6717,6731 lines. We used the $0\farcs1$ slit for the spectra passing through the nucleus and the $0\farcs2$ slit for spectra obtained through slits parallel to the one through the nucleus ($0\farcs2$ to the west and east of the nucleus). The velocity resolution of the data is $\sim$50 km s^{-1}. A summary of the information on the STIS spectra is given in Table 1.

The STIS spectra were reduced using the standard CALSTIS pipeline, built and developed by the *HST*-STIS science team.

[1] A picture displaying both Arp 102 galaxies can be viewed in *http://www.noao.edu/image_gallery/html/im0003.html*. A better display of the tidal arms can be seen in *http://www.spacebanter.com/attachment.php?attachmentid=4120&stc=1*

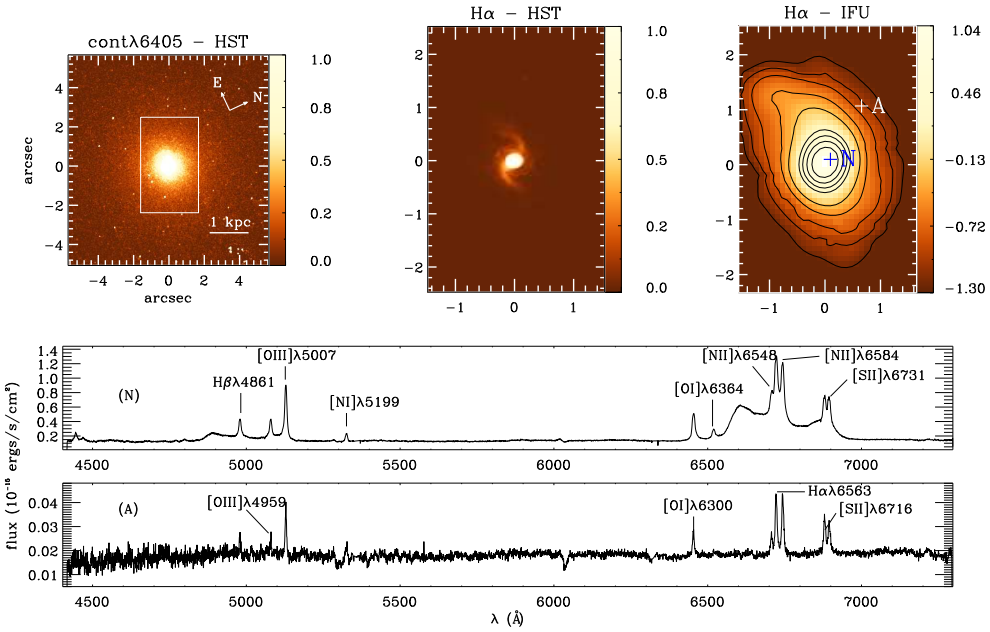

Figure 1. Top left: λ6405Å continuum map obtained with the HST ACS camera. The rectangle shows the GMOS IFU field-of-view (FOV). Top center: Hα flux map obtained with ACS within the IFU FOV. Top right: Hα flux map from the IFU spectroscopy. Bottom: Spectra extracted at the positions N (nucleus) and A marked in the top right panel.

3 RESULTS

The IFU field-of-view and data are ilustrated in Fig. 1, together with the continuum (λ6405Å) and Hα flux maps of the inner $26'' \times 29''$of Arp 102B from Paper I, obtained with the *HST*-ACS camera. In the top left panel, the rectangle shows the IFU field-of-view (FOV) oriented with its longest axis at PA=65°. In the top central panel, the HST-ACS continuum-subtracted Hα flux map shows the two spiral arms extending to ∼500 pc from the nucleus. These arms are oriented approximately to the east and west of the nucleus and we hereafter refer to them as the "east arm" and the "west arm". In the top right panel we show the Hα flux map obtained from the IFU spectroscopy. Although showing poorer spatial resolution, this map suggests that the spiral arms extend farther than seen in the *HST* image, up to ≈ 1 kpc from the nucleus. In the bottom panels we show IFU spectra extracted at the nucleus (position N) and at ≈ 1 arcsec north-east (position A), with both positions shown in the top right panel. We define the position of the nucleus as the one corresponding to the peak of the continuum emission. The nuclear spectrum shows the known broad double-peaked Hα and Hβ profiles, as well as the narrow emission lines Hβλ4861, [O III]λλ4959,5007, [N I]λ5199, [O I]λλ6300,64, [N II]λλ6548,84, Hαλ6563, [S II]λλ6717,31. All these lines – with the exception of the broad double-peaked components – are also present in the extranuclear spectrum, where they are narrower.

The STIS observations are illustrated in Fig. 2. In the top panels we show the HST Hα image within the same FOV of the IFU observations and the same orientation as Fig. 1. The slits are shown along the position angles −19.9 ° for POS1, offcen1 and offcen2 and −94.3 ° for POS2. Slits identified as POS1 and POS2 cross the nucleus, while offcen1 and offcen2 are 0.″2 offset from the nucleus. For the measurements we have extracted spectra pixel by pixel, which correspond to 0.″05 for the slits crossing the nucleus and to 0.″1 for the off-center slits. Thus along the slits crossing the nucleus the extractions correspond to apertures of $0.''1 \times 0.''05$, while for the off-center extractions the apertures are of $0.''2 \times 0.''1$. In the bottom panel of Fig. 2 we show *HST*-STIS spectra extracted at the nucleus (position N), at 0.″1 east (position A) and at 0.″2 north-west from the center of the offcen2 slit (position B). The nuclear spectrum shows the double-peaked Hα and the narrow emission lines [N II]λλ6548,84, Hαλ6563, [S II]λλ6717,31 and a weak [O I]λ6364, while the extranuclear ones show only the narrow lines.

3.1 Error estimates

In order to calculate the errors in the measurements of the line fluxes (ϵ_F), centroid velocities (ϵ_v) and widths (ϵ_σ), we applied Monte Carlo simulations to the data, adding random noise with a gaussian probability distribution, moduled by the data noise. One hundred iterations were performed for each emission line. Fig. 3 shows the errors for the flux (left panels), centroid velocity (middle panels) and velocity dispersion (right panels), measured in [O III]λ5007 (top

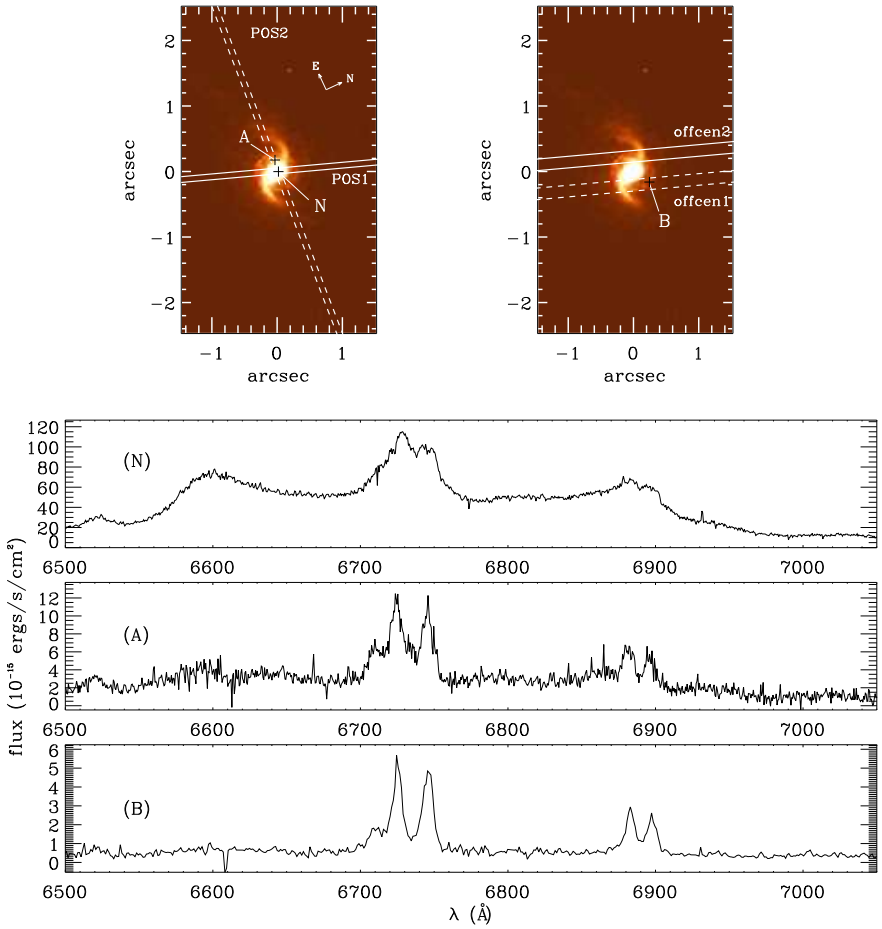

Figure 2. Top panels: continuum-subtracted *HST*-ACS Hα flux maps showing a representation of the *HST*-STIS slits. Bottom panels: Spectra extracted at positions N, A and B marked in the top panels. The flux maps have the same orientation as Fig. 1.

panels) and Hα (bottom panels). Flux errors are shown relative to the total flux in the lines ($\frac{\epsilon_F}{F}$). These error maps were used to mask out the emission-line flux distribution, centroid velocities and velocity dispersions maps, for values larger than $\frac{\epsilon_F}{F} = 0.5$ and $\epsilon_v = \epsilon_\sigma = 20\,\mathrm{km\,s^{-1}}$. Contours in Fig. 3 show the loci for which $\frac{\epsilon_F}{F} = 0.25$ and $\epsilon_v = \epsilon_\sigma = 10$ kms. We beleive these are the best values in order to distinguish good pixels, where the emission-lines are evident, from bad pixels.

3.2 Emission-line flux distributions

In order to obtain the gas emission-line fluxes and kinematics at the nucleus and surrounding regions, we had to subtract the broad-line emission from the spectra. Although the double-peaked emitting region is not resolved by our observations, the smearing of the flux due to the seeing makes the double-peaked emission contaminate the extranuclear spectra up to $\approx 0\farcs3$ from the nucleus. Using the programming language IDL[2], we have fitted three Gaussians to the Hα broad-line profile, which were then subtracted from the spectra, a procedure which efficiently eliminated the broad component.

Once we had spectra with no significant broad component, the emission-line flux distributions were obtained by fitting Gaussians to the narrow lines and integrating the corresponding flux after subtraction of the continuum contribution. In the case of the blended lines Hα+ [N II], the width of the [N II]λ6584Å and λ6548Å emission lines were constrained to the same value.

Flux maps were obtained in the emission lines of Hβ, [O III]λ5007, [N I]λ5199, [O I]λ6300, [N II]λ6584, Hα, [S II]λ6717, [S II]λ6731 and are shown in Fig. 4, together with a continuum map at λ5673, integrated within a window of

[2] Interactive Data Language, http://ittvis.com/idl

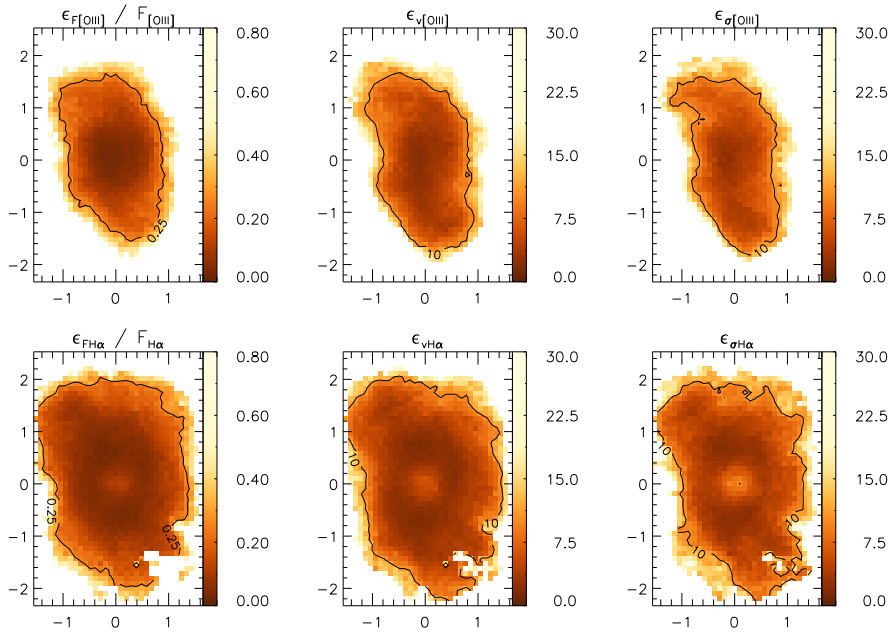

Figure 3. Monte Carlo error maps. Flux fraction (left panels), centroid velocity (middle panels) and velocity dispersion (right panels) for [O III]λ5007 (top panels) and Hα (bottom panels). Velocity units are in km s^{-1} .

100 Å. The continuum map shows little structure, with an approximately circularly symmetric flux distribution. The flux distributions in the emission lines are elongated to the east and west, showing the spiral arms first observed in the HST ACS images. The east arm is better defined and extends farther from the nucleus than the west arm for all emission lines except [O III], for which the two arms show similar extent (≈1 kpc). The green contours are from a 8.4 GHz VLA radio image (Fathi et al. 2011). Note how the radio structure follows the east spiral arm, suggesting a relation between the emitting gas and the radio structure.

3.3 Emission-line ratio maps

We have used the emission-line flux distributions to obtain the line ratio maps shown in Fig. 5. In the top left panel we show the distribution of Hα/Hβ ratios, with the highest values at the nucleus (up to ≈ 5) and lowest values (≈ 3) in regions away from the nucleus, mainly along the radio jet. The top middle panel shows that along the central part of the spiral arms, the ratio [N II]6584/Hα is almost constant at ≈ 1, increasing to larger values (≈ 1.5) towards the borders of the arms. The top right panel shows the [S II]6717/6731 emission line ratio, which shows the lowest values of ≈0.9 at the nucleus and highest values (≈1.5) towards the west. The [O III]5007/Hβ ratio (bottom left panel of Fig. 5) shows the highest values of ⩾ 4 at the nucleus, along a narrow lane running approximately perpendicular to the spiral arms and at the most distant part of the west arm. The lowest values of ≈ 1.3 are observed at ≈1″ to the east, in the "middle" of the east spiral arm, while to the west, at ≈ 0.″5 from the nucleus there is a small region with values ≈ 2. The [O I]6300/Hα ratio, shown in the bottom middle panel presents the highest values around the nucleus, mostly to north and south, with values ≈ 0.5, and lowest values (≈ 0.3) towards distant areas from the nucleus, to the east and west approximately at the locations of the spiral arms. The bottom right panel shows the ratio between the sum of the [S II] emission lines and Hα. The lowest values (≈ 0.5) are seen mainly at the nucleus and to the south, while the highest values, ≈ 1.2, are found at the locations where the [O III]5007/Hβ ratio is lowest, along the east spiral arm and at the beginning of the west spiral arm.

3.4 Gas kinematics

3.4.1 Centroid velocities and velocity dispersions - IFU

Gas velocities were obtained from the centroid wavelengths of the Gaussian curves fitted to the emission-line profiles while velocity dispersions σ were obtained from the full-width at half maximum (FWHM) of the Gaussians: σ =FWHM/2.355.

In Fig. 6 we present the centroid velocity maps (left panels) and velocity dispersion maps (right panels) for the gas emission in H α, [O III] and [S II]. The velocity values shown in Fig. 6 have had the systemic velocity $v_{sys} = 7213 \pm 2$ km s^{-1} of the galaxy subtracted. This value was calculated as the average of the centroid velocities of the Hβ, Hα and [N II] λ 6584 emitting gas in the 3 × 3 central pixels. The [N II] velocity field is very similar to that of Hα and is thus not

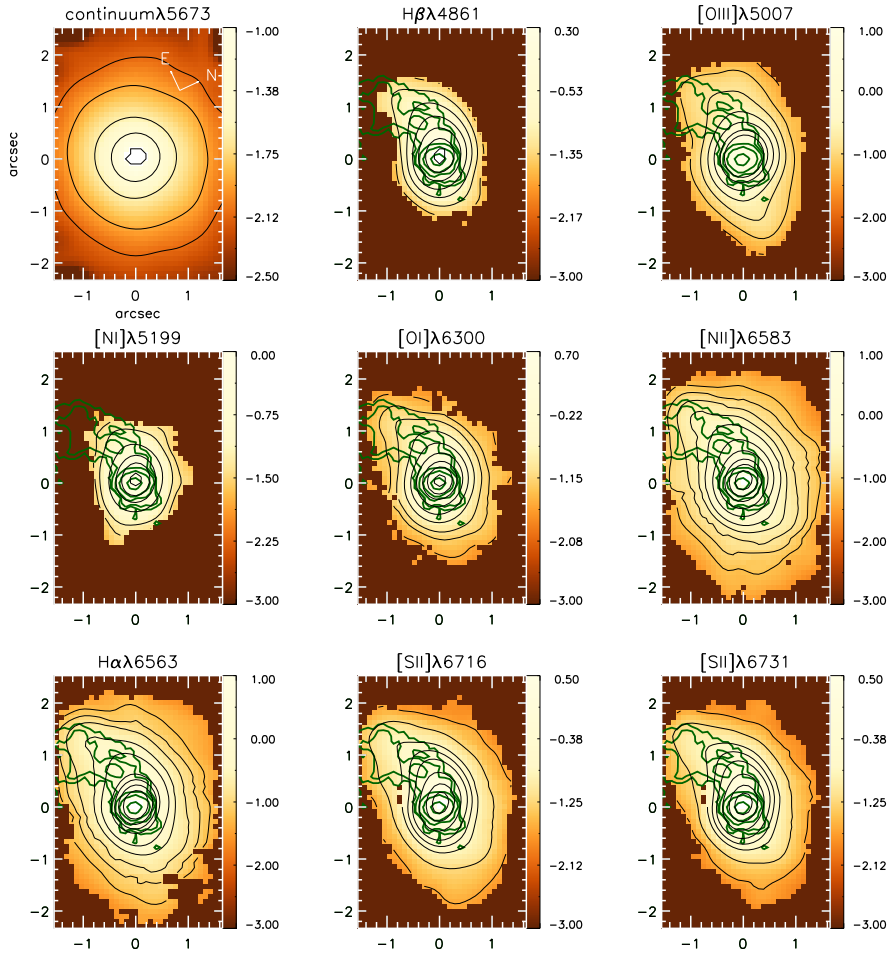

Figure 4. Flux maps in the emission lines obtained by integrating the flux under the line profiles after subtraction of the continuum contribution. Green contours are from a 8.4 GHz radio image. Flux units are 10^{-15} erg cm^{-2} s^{-1} spaxel^{-1} and are shown in a logarithmic scale.

shown. The centroid velocity maps (left panels of Fig. 6) show redshifts to the west and blueshifts to the east. The zero velocity contours show an s-shape with blueshifts to the south-east (left in the figure) and redshifts to the north-west (right in the figure).

The highest velocity dispersions ($\sigma \approx 270$ km s^{-1}) are observed around the nucleus and both to the south-east and north-west (left and right of the nucleus, respectively, in Fig. 6) for Hα and [O III], while lower values, down to ~ 100 km s^{-1} are observed elsewhere. The [S II] σ values are somewhat lower than those of Hα and [O III], reaching ≈ 200 km s^{-1}, at the same approximate locations of maximum σ-values for these lines.

The black contours in Fig. 6 show that the radio structure is mostly associated with blueshifted emission, although at the exact location of the radio emission proper, the blueshifts seem to decrease (by $\approx$ 50 km s^{-1}) relative to the surrounding regions.

3.4.2 Channel maps

We have mapped the gas kinematics using also channel maps extracted along the emission-line profiles. In Figs. 7 and 8 we show a sequence of these maps extracted within velocity bins of ~ 42 km s^{-1} and ~ 55 km s^{-1} along the Hα and [O III] emission-line profiles, respectively. They both show the highest blueshifts and redshifts at the nucleus, probably just a consequence of the high velocity dispersions there.

In the Hα channel maps (Fig. 7), the highest blueshifts outside the nucleus are observed along the east spiral arm, extending to 1.″4 (686 pc), with velocities reaching -161 km s^{-1}. Along the west spiral arm the highest redshifts are observed at similar distances from the nucleus with veloc-

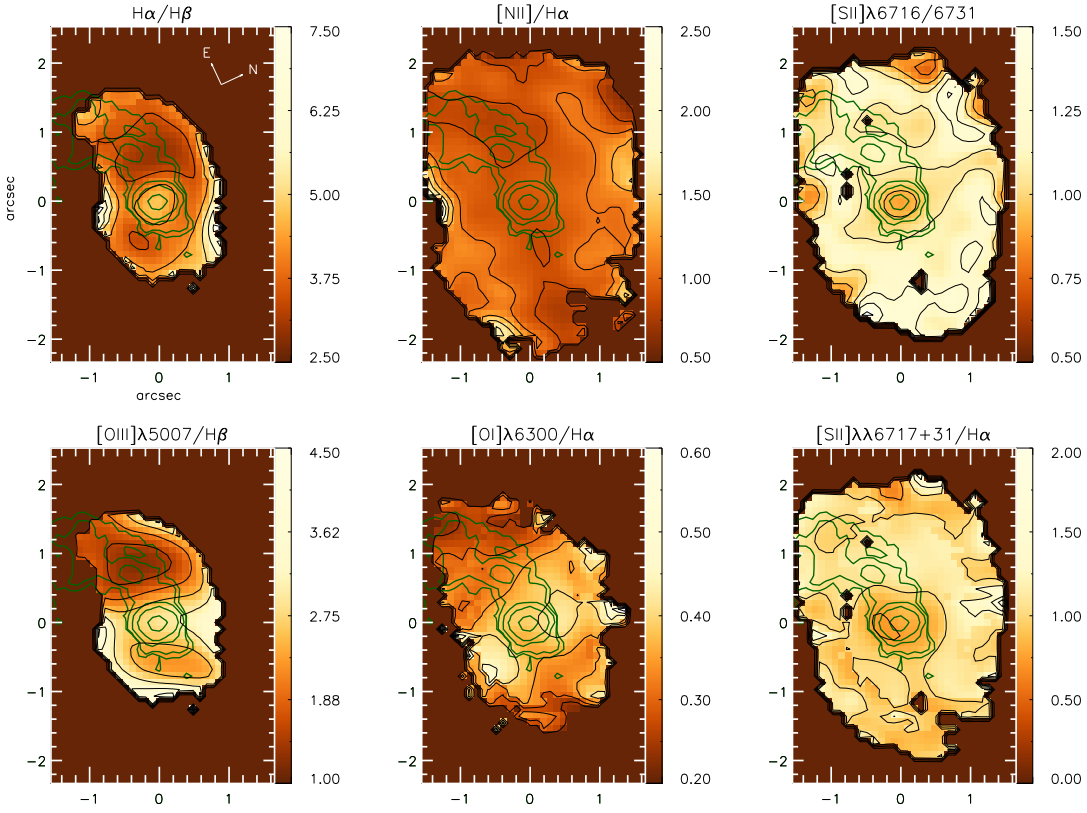

Figure 5. Line ratio maps with the green contours showing the radio structure. Top left: Hα/Hβ ratio. Top middle: [N II]6584λ/Hα ratio. Top right: [SII]$\lambda\lambda$6716/6731 emission-line ratio. Bottom left: [O III]λ5007/Hβ ratio. Bottom middle: [O I]λ6300/Hα ratio, Bottom left: [S II]$\lambda\lambda$6717+31/Hα ratio.

ities of up to 262 km s^{-1}. Even though mostly blueshifts are observed along the east spiral arm, there are also some redshifts there, reaching velocities as high as 93 km s^{-1}.

The [O III] channel maps (Fig. 8) present also high blueshifts along the east spiral arm, with velocities reaching -270 km s^{-1}. Velocities of up to 173 km s^{-1} (the highest redshift outside the nucleus) are observed along the west spiral arm. As observed for Hα, the [O III] channel maps feature redshifts as well (as high as 62 km s^{-1}) along the east spiral arm.

The green contours overlaid on the channel maps are from the radio image, supporting a correlation between the radio and the blueshifted gas emission.

3.4.3 STIS kinematics

In order to extract the gas emission-line fluxes and kinematics from the STIS spectra, we have chosen to fit both Gaussian and Lorentzian functions to the emission lines. In a few cases a Gaussian gave a better fit, in many cases, a Lorentzian gave a better fit, although the differences in the derived fluxes and kinematics were small. We decided to use the average of the results of both fits to obtain fluxes, centroid velocities and velocity dispersions, repeating the fits a few times in order to estimate the measurement errors. The measurements were accomplished using the IRAF routine SPLOT, interactively. In Fig. 9 we show the Hα flux, velocity, and velocity dispersion distributions along the slits of the STIS observations, and the corresponding error bars. Redshifts are observed along positive coordinates (north) for POS1, offcen1 and offcen2 slits, and along negative coordinates for POS2 slit (west). Blueshifts are observed to the east (POS2 slit) and south (POS1, offcen1 and offcen2 slits). High velocity dispersions are observed at the nucleus, and extend more to the east and south-east of the nucleus, while to the west and north the values decrease more abruptly. The estimated systemic velocity from the STIS data is $v_{sys} = 7385 \pm 6$ km s^{-1}, which is the average velocity for Hα emission-line of the central 5 pixels (corresponds to the central 0.″25).

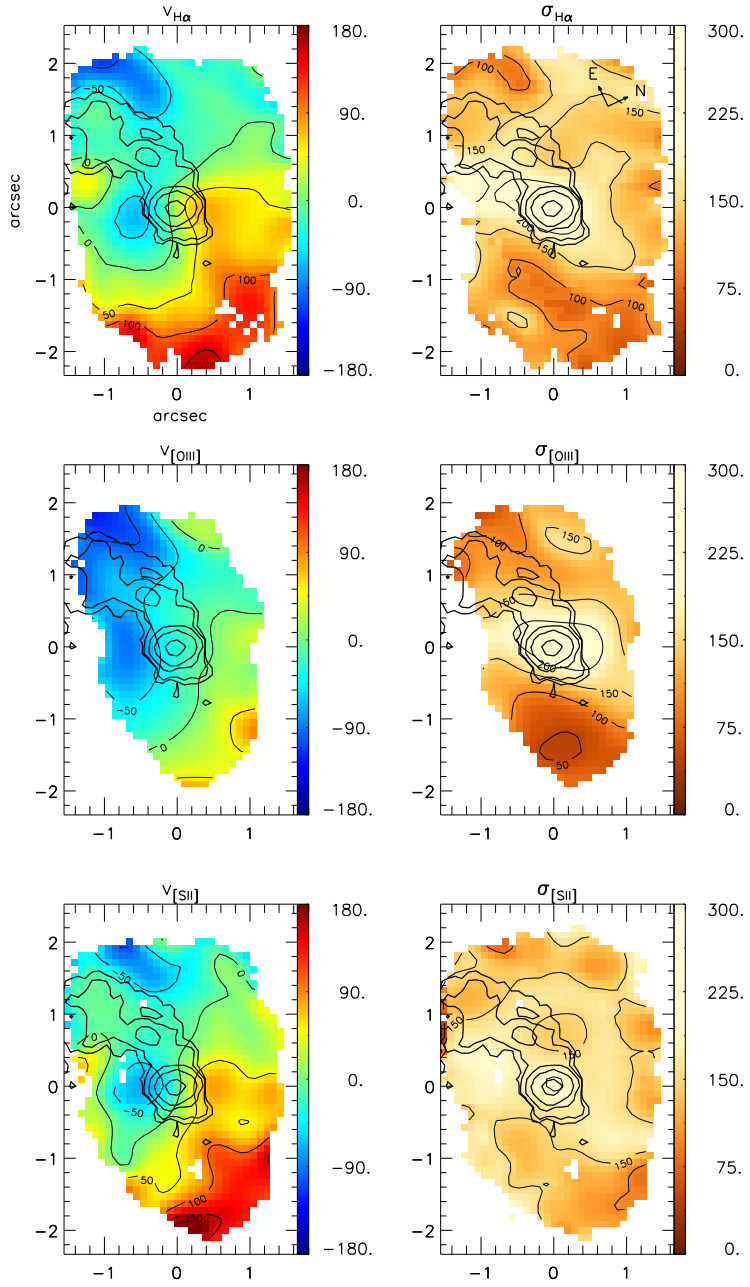

Figure 6. Centroid velocity (left panel) and velocity dispersion (right panel) maps for the emission-lines. Units are km s^{-1}.

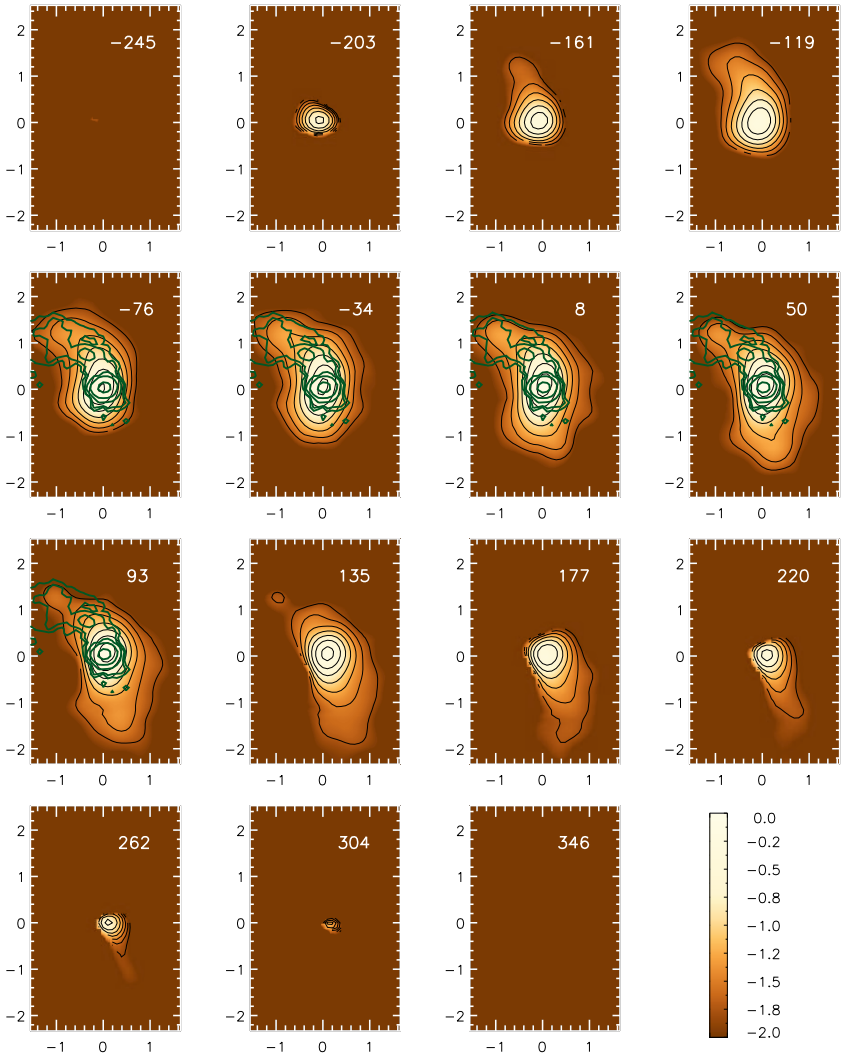

Figure 7. Channel maps along the Hα gas emission-line profile, in order of increasing velocities shown in the top right of each panel in units of km s^{-1}. Flux units are 10^{-15} erg cm^{-2} s^{-1} spaxel^{-1} and are shown in a logarithmic scale.

4 DISCUSSION

4.1 Flux distributions

Flux maps in all emission lines (Fig. 4) show the same two-armed spiral observed in the HST image of Paper I, but with the east arm being more clearly observed and extending farther from the nucleus – to at least 1 kpc from it. The west spiral arm is clearly seen in [O III]λ5007, extending to similar distances from the nucleus. For the other lines, the emission along the west spiral arm reaches approximately half the distance from the nucleus reached by the east spiral arm. As pointed out in Paper I, the VLA radio structure seems to correlate with the east spiral arm, here observed not only in Hα but also in [O III] and [S II] line emission.

4.1.1 Gas Excitation

The [N II]6584/Hα line-ratio values (top middle panel of Fig. 5) are typical of AGN excitation, being characteristic of either Seyfert or LINER nuclear activity. The [O III]5007/Hβ ratio map (bottom left panel of Fig. 5) with values ranging from $\approx$ 1.6 to $\approx$ 4.5 is more characteristic of LINER activity, although there is varying excitation, with the nucleus, north and south regions as well as the farthest part of the west spiral arm showing the highest excitation, while the re-

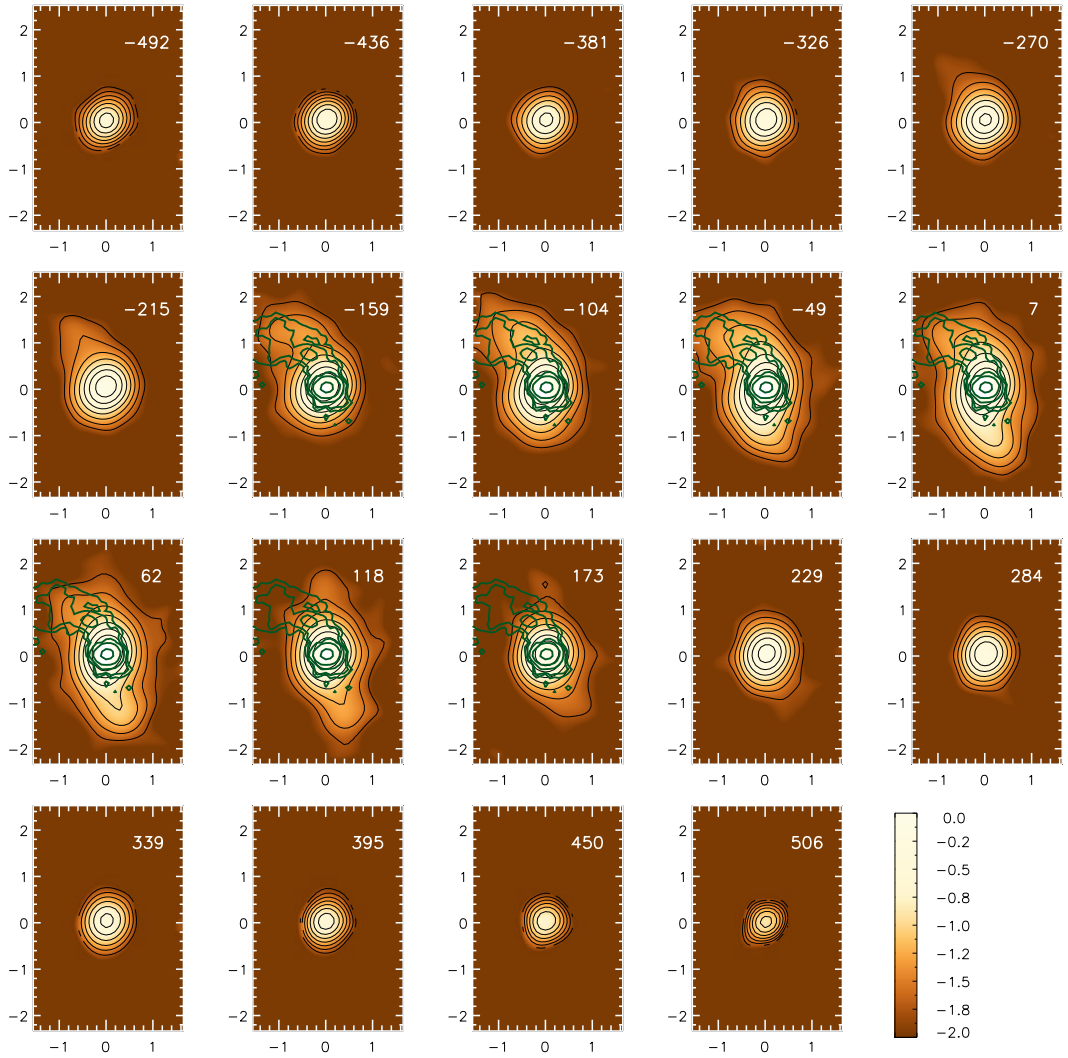

Figure 8. Channel maps along the [O III]λ5007 gas emission-line profile, in order of increasing velocities shown in the top right of each panel in units of km s^{-1}. Flux units are 10^{-15} erg cm^{-2} s^{-1} spaxel^{-1} and are shown in a logarithmic scale.

gions corresponding to the center of the east and beginning of the west spiral arms show the lowest excitation.

In order to better map the gas excitation, we have built the diagnostic diagrams (Baldwin et al. 1981) [O III]/Hβ vs. [N II]/Hα, [O III]/Hβ vs. [S II]/Hα and [O III]/Hβ vs. [O I]/Hα, shown in Fig. 10. Gray dots represent emission-line ratios from thousands of galaxy spectra in the *Sloan Digital Sky Survey* (SDSS) data (Cid Fernandes et al. 2009). Large symbols represent the Arp102B data, shown as average line ratios within the regions identified in the left panel of Fig. 10: region 1 – corresponding to an oval of 340 pc × 490 pc around the nucleus – is represented by an asterisk; region 2 – oval of 200 pc × 290 pc at 290 pc north-west of the nucleus – is represented by a triangle; region 3 – an oval of 590 pc × 200 pc at 250 pc west of the nucleus, at the beginning of the west spiral arm – is represented by a circle and region 4 – oval of 690 pc × 440 pc at 440 pc east of the nucleus, in the middle of the east spiral arm – is represented by a square. Symbols sizes are of the order of the error bars, estimated by the standard deviation.

The dashed lines, obtained from Kewley et al. (2006), are the dividing lines between HII-type galaxies (left) and active galaxies (right). Higher [O III]/Hβ values in the AGN side characterize Seyfert nuclei, and lower values characterize LINERs. Arp 102B ratios are clearly located in the AGN side in the three diagnostic diagrams. The [O III]/Hβ ratio

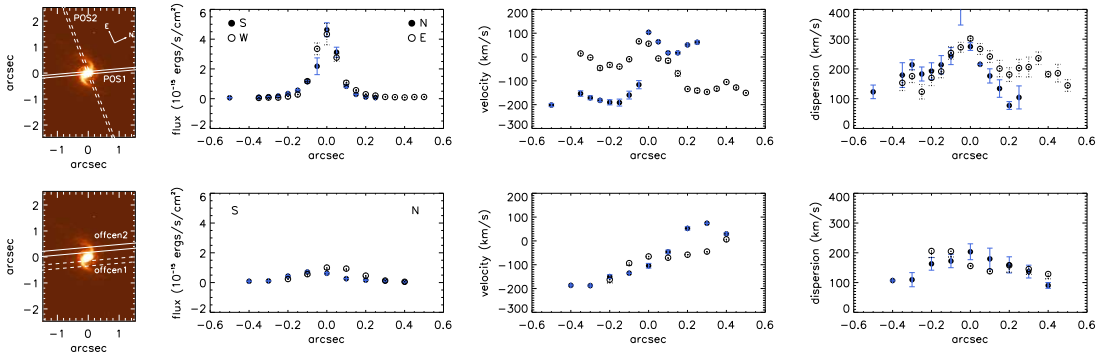

Figure 9. Hα flux, velocity, and velocity dispersion derived from STIS spectra. The filled symbols show values along POS1 (PA=−19.9 °) in the top panel, and empty symbols those along POS2 (PA=−94.3 °). In the bottom panel, filled symbols correspond value along offcen2, and empty symbols alond offcen1. The velocities are plotted around the systemic velocity v_{sys} = 7385 km s^{-1}. Error bars are derived from both gaussian and lorentzian fitting, and the values represent the mean value. Legends show the orientation along the plots.

values are mostly in the LINER region, although very close to the Seyfert loci, in particular for the extranuclear region 2, in agreement with the LINER/Seyfert 1 classification. The nuclear (region 1) line ratios are very similar to those of region 3 (beginning of the west arm), and are closer to the LINER region, while region 4, in the middle of the east arm is in the LINER region.

Although the lower values of the [O III]/Hβ ratio map in the east spiral arm (and in the beginning of the west spiral arm) could be due to the presence of HII regions, the loci of the corresponding data points in the diagrams do not support this interpretation, favoring instead ionization by a diluted continuum and/or the contribution of shocks along the east and west spiral arms.

4.1.2 Gas reddening and density

We have used the observed Hα/Hβ line ratio (Fig. 5) to calculate the gas reddening. Adopting the Cardelli, Clayton & Mathis (1989) reddening law, and assuming case B recombination (Osterbrock & Ferland 2006) we obtain

$$E(B-V) = 2.22 \log \frac{(\frac{H\alpha}{H\beta})}{3.1}. \quad (1)$$

The corresponding reddening map is shown in the left panel of Fig. 11. The highest reddening values (E(B-V)$\geqslant$0.4) are observed at the nucleus and both to the south-east and north-west of it. The smallest reddening values, close to 0, are observed at $\approx 1''$ from the nucleus, in the middle of the east spiral arm, surrounded by regions with (E(B-V))$\approx$ 0.25, a value observed also in the beginning of the west spiral arm. This map suggests that the spirals – and the radio jet – may have cleared a channel in the beginning of the arms pushing away the dust along the way.

We have used the ratio of the [S II] emission lines (top right panel of Fig. 5) to calculate the gas density (Osterbrock & Ferland 2006), whose map is displayed in the right panel of Fig. 11. The temperature used to estimate the gas density is 10,000 K. The highest density values of $\approx$900 cm^{-3} are observed at the nucleus, approximately co-spatial with the location of highest reddening. Away from the nucleus, the highest densities are observed along the east spiral arm, with an average value of about 500 cm^{-3}, but presenting two knots of higher density values at its northern and east borders. These knots seem to bound the region covered by the bent radio jet. In particular, a radio knot at 0.″8 east of the nucleus occurs adjacent (below in Fig. 11) to a high-density knot, suggesting that this high density knot may have deflected the radio jet, leading to its bent appearance.

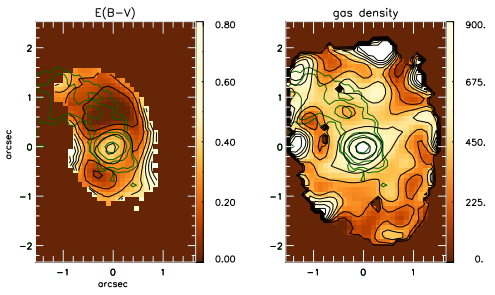

Figure 11. Reddening map, with values of E(B-V) obtained from the Hα/Hβ ratio, and gas density maps, derived from the [S II] ratio. Density units are cm^{-3}.

The presence of high density knots along the east spiral arm, as well as the radio knot 0.″8 east of the nucleus, combined with the high velocity dispersions observed along the east arm up to the radio knot (right top and middle panels of Fig. 6) support at least some contribution from shocks to the gas ionization in this region, leading to LINER-like emission-line ratios.

The gas excitaton with LINER-like line ratios could be due to shocks or diluted radiation. Although the velocity dispersion maps shows no unusual high values in the region, the scenario including shocks cannot be ruled out, once the dispersion is not negligible along the spiral arms. We have

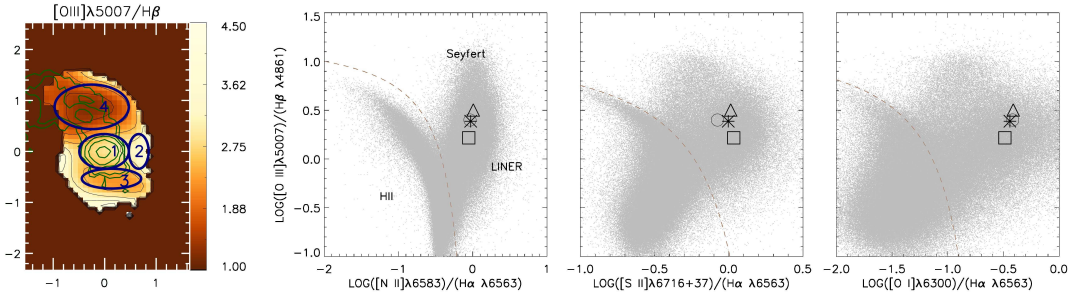

Figure 10. Diagnostic diagrams in which the small gray dots represent ratios obtained from SDSS emission-line galaxies spectra. The dashed line divides the loci of HII-type galaxies (left) from that of AGNs (right). Symbols represent regions displayed in the [O III]5007/Hβ ratio map (left panel). Region 1 is represented by an asterisk, region 2 by a triangle, region 3 by a circle and region 4 by a square.

also considered the possibility that the low [O III]/Hβ values were due to the presence of a star forming region in the east spiral arm, but this hypothesis can be discarded, as the high [N II]6584/Hα and [O I]6584/Hα ratios are much larger than those observed in HII regions.

4.2 Gas Kinematics

Fig. 6 shows that the centroid velocity fields suggest rotation, with redshifts to the west and blueshifts to the east. Nevertheless, the isovelocity curves are distorted relative to the well known "spider diagram" (characteristic of rotation), and a possible interpretation is a combination of gas rotation and outflow. The aparent s-shape of the central isovelocity curves could be due to the presence of what seems to be a "blob" of blueshifted line emission at $\approx 0\farcs7$ south-east of the nucleus (to the left of the nucleus in Fig. 6) with negative velocities in excess of $-50\,\mathrm{km\,s^{-1}}$ in the Hα centroid velocity map. This "blob" could be interpreted as due to an outflow which could also explain the high velocity dispersions observed at its location. Although not conspicuous in the channel maps as a detached structure, the blueshifted channel maps between velocities ≈ -150 and $-50\,\mathrm{km\,s^{-1}}$ do show an extension to the south-east, at the location of this blob.

Another interesting feature of the centroid velocity maps is a region of lower blueshifts – co-spatial with the radio jet – surrounded by higher blueshifts. In the channel maps we see that although the jet region is dominated by blueshifts, there are also some redshifts observed at the same locations. This could be due to a broad outflow launched close to the plane of the sky, with the front part approaching and the back part receeding, but slightly tilted toward us, so that the centroid velocities would still show blueshifts, but lower than the surrounding rotation velocities. Thus the highest blueshifts to the east and highest redshifts to the west could be due to rotation, while the intermediate blueshifts and redshifts to the east would include the contribution from the front and back walls of the outflow.

4.2.1 Velocity rotation modelling

In order to try to separate the contributions of possible rotation and outflow to the velocity field, we fitted a rotation model to the Hα centroid velocity map, assuming that the emitting gas is rotating in a central potential, as we have done in previous works (Barbosa et al. 2006; Riffel et al. 2008; Schnorr Müller et al. 2011). In this kinematic model (Bertola et al. 1991; van der Kruit & Allen 1978) it is assumed that the gas has circular orbits in a plane, and the rotation field is given by

$$v_{mod}(R,\Psi) = v_{sys} + \frac{AR\,cos(\Psi-\Psi_0)\,sin\theta\,cos^p\theta}{\{R^2[sin^2(\Psi-\Psi_0)+cos^2\theta\,cos^2(\Psi-\Psi_0)]+c_0^2\,cos^2\theta\}^{p/2}} \quad (2)$$

where v_{sys} is the systemic velocity, A is the centroid velocity amplitude, Ψ_0 is the major axis position angle, c_0 is a concentration parameter, θ is the disk inclination relative to the plane of the sky, p is a model fitting parameter (which is ~ 1 for finite masses in a Plummer potential) and R and Ψ are the coordinates of each pixel in the plane of the sky. Fig. 12 shows in the first three panels the measured Hα centroid velocity map, the resulting model of rotation curve and the residual between both, respectively. The red dashed box shown encloses the "blueshifted blob", which is found in the centroid velocity maps. Since this region seems to show the most significant deviations from a rotation pattern, we decided to mask it out of the fit. The resulting parameters are: $A \approx 268 \pm 8\,\mathrm{km\,s^{-1}}$, $v_{sys} \approx 7244\,\mathrm{km\,s^{-1}}$, $\Psi_0 \approx 88^\circ$, $c_0 \approx 5$ arcsec and $\theta \approx 79^\circ$ (error bars in almost all parameters are smaller than unity, then not shown here). We fixed the center of the rotation curve in $x_0 = 0$ and $y_0 = 0$ arcsec, with $p = 1$. The systemic velocity resulting from the modelling is close to the average value we adopted as systemic (Sec. 3.4.1) and both are in agreement with de Vaucouleurs et al. (1991) ($7245 \pm 34\,\mathrm{km\,s^{-1}}$). Fig. 12 shows the observed velocity map in the left panel, the model velocity field in the center panel, and the residual between the two in the right panel.

The masked region is the only one with values larger than $40\,\mathrm{km\,s^{-1}}$ in the residual map. This indicates that our hyphotesis of combined rotation and outflow in the blueshifted "blob" is a good representation of the data. A small redshifted region in the residual map (residuals of $\approx 40\,\mathrm{km\,s^{-1}}$), located to the right (north-west) of the nucleus, suggests the presence of a redshifted blob which could

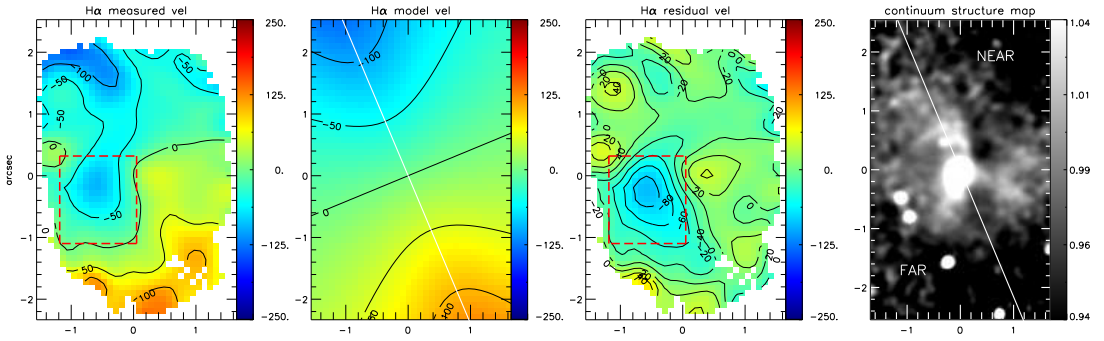

Figure 12. Gas rotation model for H α. Left: the measured centroid velocity map. Middle left: model of the rotation curve. Middle right: residual map. Right: structure map. The red dashed box illustrates the masked region due to high residual velocities, from a possible outflow. The white line displays the position of the line of nodes. Velocities are in km s^{-1} .

be the counterpart for the blueshifted "blob", in the hypothesis they are due to a bipolar outflow.

Fig. 12 shows that the rotation model is a good representation of the gas centroid velocity kinematics, and that the disk seems to be very inclined. In order to try to determine which is the near and far sides of the disk, we have looked for possible signatures of dust obscuration, which is usually larger in the near side of an inclined disk.

Dust lanes can be highlighted via structure maps (Pogge & Martini 2002; Simões Lopes et al. 2007), in which high contrast regions – such as those resulting from dust obscuration or high emission structures – can be enhanced, appearing as dark and bright regions, respectively. The right panel of Fig. 12 shows the structure map we have obtained from the HST ACS continuum image shown in Fig. 2. A dark lane to the north-east of the nucleus running approximately east-west (passing to the right of the nucleus in the figure) could be due to extinction by dust in the near side of a highly inclined disk.

The dust lane thus seems to support a high inclination for the rotating disk, as derived from our rotation model (79°). And suggest that the spiral arms are not all in the disk, as they would not be visible at such high inclination. Our hypothesis is that the jet is launched close to the plane of the sky and of the line of nodes of the rotating disk, then suffers a deflection to high latitudes relative to the rotating gas disk, dragging along gas from the disk.

In order to have more elements to interpret the overall kinematics, we decided to apply a PCA analysis to the IFU data (Steiner et al. 2009) in a similar way as described in the previous study by members of our group of the gas kinematics of the nuclear region of M81 (Schnorr Müller et al. 2011).

4.2.2 PCA Analysis

The PCA is applied directly to the calibrated datacube separating the information, originally presented in a system of correlated coordinates, into a system of uncorrelated coordinates ordered by principal components of decreasing variance. These new coordinates called "eigenspectra" reveal spatial correlations and anti-correlations in the emission-line data. The projection of the data onto these new coordinates produce images called "tomograms", which map the spatial distribution of the eigenspectra.

The result of the PCA is shown in Fig. 13. From top to bottom the panels show the tomograms (to the left) and respective eigenspectra (to the right), in order of decreasing variance.

Component PC1, which carries the largest variance (97.9%), shows an eigen-spectrum dominated by the AGN and the stellar continuum contribution, represented by the positive values in the eigenspectrum and showing a circularly symmetric spatial distribution in the corresponding tomogram.

Component PC2 is dominated by the contribution of the broad-line emission, originating in the nucleus and extending about 0.6 arcsec due to seeing – the red region of the tomogram, being spatially anti-correlated with the stellar population, which originates from the blue region (circumnuclear region) in the tomogram. The anti-correlation is revealed by the inverted stellar population features (which appear in emission) in the eigenspectrum (e.g. the NaIλ5890 and Mgλ5175 absorption features characteristic of stellar populations).

Most important for the nature of the emission-line gas are components PC3 and PC4. PC3 shows narrow lines anti-correlated with the broad component of Hα. This broad component appears in red in the tomogram, corresponding to positive values and originates in the nucleus, as expected. Narrow lines appear as absorptions in the eigenspectrum, corresponding to blue regions in the tomogram. The emission-lines thus originate in the two blobs, one more extended to the east and one less extended to the west of the nucleus, coinciding with the location of the beginning of the spiral arms. Notice that there is no velocity gradient in the emission lines, meaning that the two blobs originate in gas at similar velocities. One possibility is that these blobs are due to gas being ejected close to the plane of the sky. This result supports the hypothesis put forth in the previous section that the jet is launched close to the plane of the sky (approximately along the major axis of the rotating disk) and that these blobs correspond to the inner parts of the outflows pushed by the radio jet.

The PC4 eigenspectrum shows the narrow lines with components in blueshift (negative values), spatially anti-correlated with components in redshift (positive values). The tomogram shows that the components in blueshift originates to the left of the nucleus, while the redshifted component originates to the right of the nucleus. This pattern leaves us two possible interpretation: gas rotation or a bipolar outflow. The blueshifted region is very well aligned with the blueshifted "blob". The counterpart structure observed in redshift has also been previously seen in the residual map of the velocity rotation model. Both regions show also high velocity dispersion, supporting the interpretation that they are due to another bipolar outflow, almost perpendicular to the radio jet. Two sets of perpendicular outflows are also seen in Markarian 6 (Kharb et al. 2006). This could be the case here: we are seeing a new outflow perpendicular to the firts due to precession of a nuclear jet. In fact, Seyfert galaxies have short- lived outflows (10^4-10^5 years) since the SMBH spin-axes change frequently and the accretion disks are short-lived (Sikora et al. 2007).

4.2.3 Comparison between the STIS and IFU kinematics

The IFU data allows the two-dimensional mapping of the gas kinematics up to ≈ 1 kpc from the nucleus, while the STIS data provides one-dimensional coverage in only two position angles, reaches smaller distances from the nucleus, but probes a finer spatial scale. In Fig. 14 we compare the Hα kinematics obtained from the IFU data to the one obtained from the STIS data (Fig. 2). In order to do this, we have extracted pseudo-slits from the IFU datacube, with the same orientation as the STIS slits.

Error bars were obtained for the IFU data by performing multiple fits to the Hα emission line, and resulted smaller than the circles representing the data points, except for the farthest regions from the nucleus. In order for the velocities to overlap we had to subtract $60\,\mathrm{km\,s^{-1}}$ from the centroid velocities obtained from the IFU data. We attribute this difference to a distinct zero point in the wavelenght calibration of the two datasets. The kinematics obtained from the IFU data seems smoothened as compared with the one obtained from the STIS data, due to the lower spatial resolution of the ground-based data when compared to STIS data. Despite this difference in resolution, there is reasonable agreement between these two sets of data, both in centroid velocities and velocity dispersions.

The pattern seen in the STIS data matches the one observed in the centroid velocity curves obtained with IFU, with blueshifts to the east and south and redshifts to the west and north. The blueshifted "blob" to the left of the nucleus, previously discussed, is also noticed with the higher definition STIS data, with high negative velocities between $0\farcs0$ and -$0\farcs5$.

Although the STIS data reaches only up to $0\farcs5$ from the nucleus, it shows, in the velocity dispersion diagrams, that high values are found to the south-east (left of the nucleus in the images), in agreement with the kinematics derived from the IFU observations.

4.3 One-sidedness mechanisms in radio jets

In Paper I, we attributed the one-sidedness of the radio jet of Arp 102B to relativistic boosting. Even though our IFU observations favor a scenario where the jet is being launched close to the plane of the sky, we should still consider the interpretation of relativistic boosting, since we observe a bending of the jet about $\approx 0\farcs5$ from the nucleus, probably towards our line-of-sight.

It is possible, if the twin jets have different intrinsic powers, that an asymmetric density distribution in the surrounded interstellar medium can cause a disruption of the counter-jet. This could be supported by our density map (Fig. 11), as long as this occurs within few hundred parsecs from the nucleus, where the gas density is highest. Nevertheless, our data seems unsufficient to distinguish between these models. Further radio observations, perhaps in several frequencies, would better constrain these possibilities.

4.4 Mass of the emitting gas

We estimated the mass of the ionized gas as:

$$M = V \epsilon n_e m_p \,, \tag{3}$$

where V is the volume of the emitting region, ϵ is the filling factor, n_e is the electron density and m_p is the proton mass.

From Osterbrock & Ferland (2006), the emissivity of the Hβ line can be calculated as:

$$j_{H\beta} = n_e n_p \alpha^{eff}_{H\beta} \frac{h\nu_{H\beta}}{4\pi} \,, \tag{4}$$

where n_p is the proton density, $\alpha^{eff}_{H\beta}$ is the $H\beta$ effective recombination coefficient and $h\nu_{H\beta}$ is the corresponding energy. When integrated over the entire emitting volume and over all directions, the emissivity gives us the total luminosity in Hβ:

$$L(H\beta) = \iint j_{H\beta}\,\mathrm{d}\Omega\,\mathrm{d}V = 1.2\times10^{-25}\,V\,\epsilon\,n_e^2\,\mathrm{erg\,s^{-1}} \,, \tag{5}$$

where we use the approximation that the gas composition is pure hydrogen and it is completely ionized ($n_e \equiv n_p$), and we adopted the $\alpha^{eff}_{H\beta}$ for a temperature of 10^4 K. We can then obtain:

$$V\,\epsilon = 8.1\times10^{59}\,\frac{L_{41}(H\beta)}{n_3^2}\,\mathrm{cm^{-3}} \,, \tag{6}$$

where $L_{41}(H\beta)$ is the Hβ luminosity in units of 10^{41} ergs $\mathrm{s^{-1}}$ and n_3 is the electron density in units of 10^3 $\mathrm{cm^{-3}}$. The estimated mass of the emitting region comes from the introduction of equation 6 into equation 3, which gives:

$$M \approx 7\times10^5\,\frac{L_{41}(H\beta)}{n_3^2} M_\odot \,. \tag{7}$$

This calculation in further details can be seen in Peterson (1997).

In order to calculate the total Hβ luminosity, we needed to correct the integrated Hβ flux, $F(H\beta)$, for redenning. We used the reddening law of Cardelli, Clayton & Mathis (1989):

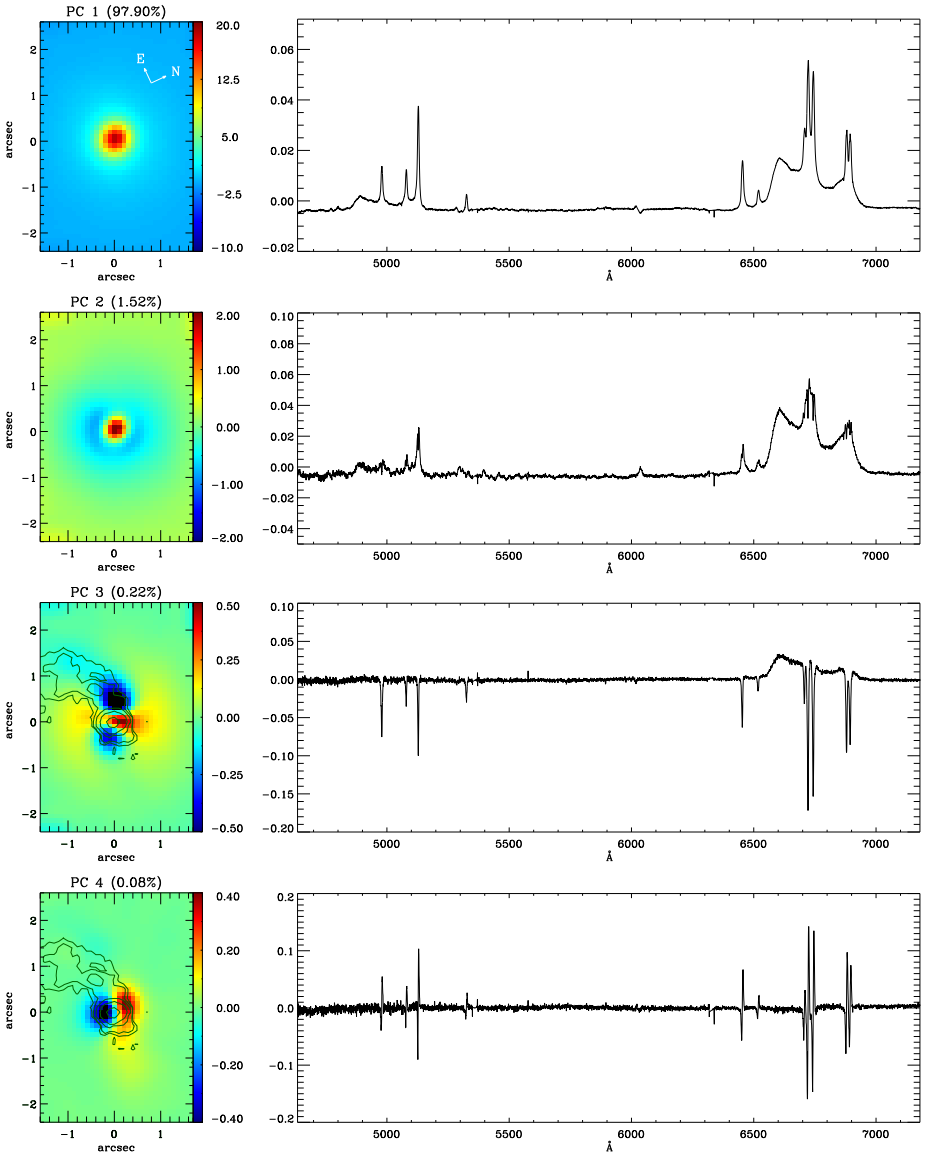

Figure 13. PCA Analysis. From up to bottom: tomograms (left) and eigenspectra corresponding to PC1, PC2, PC3 and PC4, in decrescent order of variance.

$$\frac{F(H\alpha)}{F(H\beta)} = \frac{F_0(H\alpha)}{F_0(H\beta)}\, 10^{-C(H\beta)\frac{f(H\alpha)-f(H\beta)}{f(H\beta)}}\,, \qquad (8)$$

where $F(H\alpha)$ is the integrated Hα flux, $\frac{F_0(H\alpha)}{F_0(H\beta)}$ is the corrected flux ratio, $C(H\beta)$ is the interstellar extinction coefficient and $f(H\alpha)$ and $f(H\beta)$ are the interstellar extinction function values for Hα and Hβ, respectively. We adopted the theoretical values given in Osterbrock & Ferland (2006), $f(H\alpha) = 0.818$, $f(H\beta) = 1.164$ and $\frac{F_0(H\alpha)}{F_0(H\beta)} = 3.0$, which correspond to case B recombination. With the integrated fluxes ($F(H\alpha) = 3.8 \pm 0.3 \times 10^{-15}$ ergs cm^{-2} s^{-1} and $F(H\beta) = 5.2 \pm 1 \times 10^{-16}$ ergs cm^{-2} s^{-1}) we calculate a value of $C(H\beta) = 1.3 \pm 0.3$. For the assumed distance of 104.9 Mpc, we have:

$$L(H\beta) = 4\pi d^2 F(H\beta) 10^{C(H\beta)} = 1.4 \pm 1 \times 10^{40}\,\mathrm{ergs\,s^{-1}}\,. \qquad (9)$$

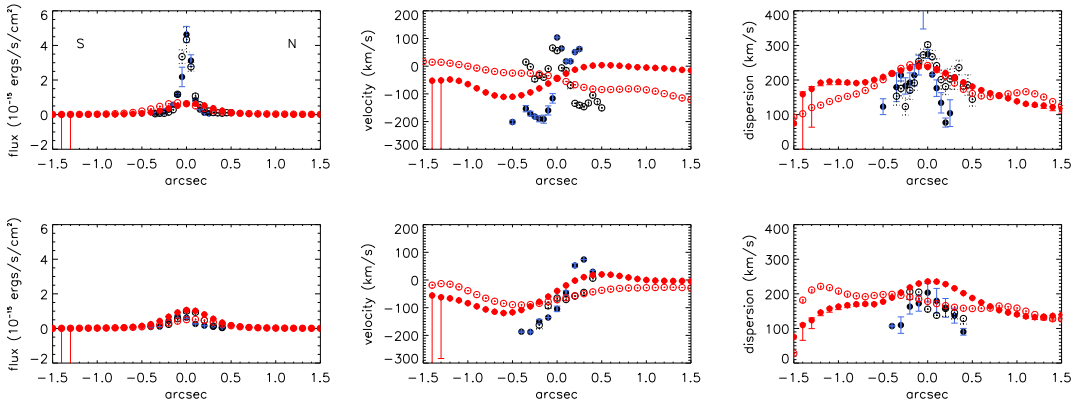

Figure 14. Comparison between the Hα kinematics obtained form the STIS data and from the IFU data. The format is the same as Fig. 9, but with the IFU data included as red circles.

Using an average electron density $n_3 \approx 0.33$ we obtain a mass of the emitting gas of $M = 2.9 \pm 2 \times 10^5 M_\odot$.

4.5 Mass outflow rate

In the analysis of the gas kinematics, we found evidence for an outflow associated with the radio jet along the east spiral arm and reaching ≈ 1 kpc ($2\farcs0$) from the nucleus, and another one causing the blueshifted "blob" at ≈ 350 pc ($0\farcs6$) south-east from the nucleus. In this section we estimate the mass outflow rate for the first, stronger outflow, as it seems to have a much larger associated mass.

In order to estimate the mass outflow rate, we need to adopt a geometric parameters for the outflow. The derivation of such parameters is a hard task, once there are projection effects and the outflow geometry is not clear. We have assumed an approximately cylindrical geometry for the outflow, that opens up somewhat with increasing distance from the nucleus, bending towards our line of sight. The outflow projected width and height can be estimated from the radio image contours before the bending of the structure: width of $\approx 0\farcs8$ at ≈ 1 arcsec east of the nucleus, and reaching about $\approx 2\farcs0$ from the nucleus. Assuming $0\farcs8$ ($= 392$ pc) to be the diameter of a circular cross-section of the outflow, its area is $A = \pi r^2 = 1.1 \times 10^{42}\,\mathrm{cm}^{-2}$. The mass outflow rate can be calculated as (Riffel & Storchi-Bergmann 2011):

$$\dot{M}_{out} = m_p\, n_e\, v_{out}\, A\, \epsilon\,, \qquad (10)$$

where, $m_p = 1.7 \times 10^{-24}$ g is the proton mass, $n_e = 330\,\mathrm{cm}^{-3}$ is the electron density (calculated as explained in the last section), v_{out} is the velocity of the outflow perpendicular to A at $\approx 1\farcs0$ east of the nucleus and ϵ is the filling factor.

In order to estimate the velocity of the outflow, we have used Fig. 7 and considered that the outflow contributes to the channels with velocities ranging from $-161\,\mathrm{km\,s}^{-1}$ to $135\,\mathrm{km\,s}^{-1}$. We have calculated the velocity of the outflow as an average of the velocities of these channels weighted by their corresponding fluxes, which results in $v_{out} \approx -25\,\mathrm{km\,s}^{-1}$. Now we need to know the orientation of the outflow relative to the line-of-sight. Chen & Halpern (1989), in their accretion disk model to reproduce the double-peaked Hα profile calculated an angle of 33° for the inclination of the accretion disk. One possibility is that we assume this inclination for the disk and that the jet is launched perpendicularly to the accretion disk, making an angle of 57° with the plane of the sky. This gives a deprojected outflow velocity of $v_{out} \approx -30\,\mathrm{km\,s}^{-1}$. The total flux emitted by the estimated outflow is $F(H\beta) = 9.1 \times 10^{-15}\,\mathrm{erg\,cm}^{-2}\,\mathrm{s}^{-1}$ and a luminosity of $L(H\beta) = 4\pi d^2\, F(H\beta) = 1.2 \times 10^{40}\,\mathrm{erg\,s}^{-1}$. With the geometry assumed, which results in $V = 3.5 \times 10^{63}\,\mathrm{cm}^3$, we obtain a filling factor of $\epsilon = 2.6 \times 10^{-4}$, using equation 6. With these assumptions, we obtain a mass outflow rate of $\dot{M}_{out} = 7.8 \times 10^{-3}\,\mathrm{M}_\odot\,\mathrm{yr}^{-1}$.

Nevertheless, the observed geometry and low velocity for the outflow, as well as the PCA results, suggest that the angle between the outflow and the plane of the sky is much smaller than 57°. The fact that both blueshifts and redshifts are observed in the region of the outflow, with a small excess of blueshifts suggests that the central axis of the outflow is tilted towards us, but part of the outflow must be moving away from us. Considering that the outflow geometry is the one inferred from the radio contours, assuming cylindrical symmetry we conclude that the angle between the axis of the outflow and the plane of the sky is $\leqslant 14^\circ$. Using and angle of 10° a deprojected outflow velocity of $v_{out} \approx -146\,\mathrm{km\,s}^{-1}$ and a mass outflow rate of $\dot{M}_{out} = 3.8 \times 10^{-2}\,\mathrm{M}_\odot\,\mathrm{yr}^{-1}$.

We can then compare the outflow mass rate with the accretion rate, calculated as (Peterson 1997):

$$\dot{m} = \frac{L_{bol}}{c^2\,\eta} \approx 1.8 \times 10^{-3} \left(\frac{L_{44}}{\eta}\right) \mathrm{M}_\odot\,\mathrm{yr}^{-1}\,, \qquad (11)$$

where L_{bol} is the nuclear bolometric luminosity, c is the light speed, η is the efficiency of conversion of the rest mass energy of the accreted material into radiation power and L_{44} is bolometric luminosity in units of $10^{44}\,\mathrm{erg\,s}^{-1}$. As in Riffel & Storchi-Bergmann (2011), we calculated $L_{bol} \approx 100\,L(H\alpha)$,

where $L(H\alpha)$ is the nuclear luminosity in Hα. Integrating Hα nuclear flux within our angular resolution ($0\farcs5$), we obtain $F(H\alpha) = 2.5\times10^{-15}$erg cm^{-2} s^{-1}, which leads to an Hα luminosity of $L(H\alpha) = 4.2 \times 10^{41}$erg s^{-1}, calculated as the previous section. With this values we obtain a bolometric luminosity of $L_{bol} = 4.2 \times 10^{43}$erg s^{-1}.

Assuming an efficiency of an optically thick and geometrically thin accretion disk (Frank, King & Raine 2002), $\eta \approx 0.1$, we derive an accretion rate of $\dot{m} = 7.5 \times 10^{-3}\,M_\odot\,yr^{-1}$, which is just somewhat smaller than the mass outflow rate.

We can finally use the mass outflow rate to estimate the outflow kinetic power as (Storchi-Bergmann et al. 2010; Riffel & Storchi-Bergmann 2011):

$$\dot{E} \approx \frac{\dot{M}_{out}}{2}(v_{out}^2 + \sigma^2)\,, \qquad (12)$$

where σ is the velocity dispersion. Using an average velocity dispersion measured in Hβ, $\sigma \approx 175\,km\,s^{-1}$, $v_{out} \approx 30 - 146\,km\,s^{-1}$ and $\dot{M}_{out} \approx 0.8 - 3.8 \times 10^{-2}\,M_\odot\,yr^{-1}$, we derive a kinetic power of $\dot{E} \approx 0.8 - 6.2 \times 10^{38}$ ergs s^{-1}, $\dot{E} \approx 0.2 - 1.5 \times 10^{-3}\%$ when compared to the bolometric luminosity L_{bol}.

5 CONCLUSIONS

We have measured the gas excitation and kinematics in the inner $2.5 \times 1.7\,kpc^2$ of the LINER/Seyfert 1 galaxy Arp 102B from optical spectra obtained with the GMOS integral field spectrograph on the Gemini North telescope with a spatial resolution of 245 pc at the galaxy. Our main goal was to investigate the nature of the nuclear spiral arms discovered in Paper I. Our measurements and analysis have shown that:

(i) the gas emission is enhanced in the nuclear spiral arms, although being observed at lower intensity also outside the arms;

(ii) the gas density is higher along the arms when compared to gas outside the arms, showing knots with even larger densities at the northern border of the east arm in the region where the radio jet seems to be deflected;

(iii) the gas along the arms shows the lowest excitation, typical of LINERs, with line ratios which are not compatible with ionization by stars, precluding the presence of HII regions in the arms;

(iv) the LINER-like ratios, combined with a high velocity dispersion at the base of the arms, support the interaction of the jet with the circum-nuclear gas in the east arm, as well as contribution from shocks to the gas excitation;

(v) the gas centroid velocities over most of the field-of-view are well described by rotation in a disk, but there is a clear spatial correlation between the radio jet, the east spiral arm and a lower centroid velocity, supporting an interaction between the radio jet and circumnuclear gas;

(vi) in the channel maps, at the location of the east spiral arm and jet, there are both blueshifts and redshifts, which can be interpreted as due to an outflow occurring close to the plane of the sky, tilted towards us by an angle $\approx 10^\circ$, so that the front part of the outflow is observed in blueshifts but part of the back is observed in redshift;

(vii) the emitting gas mass calculated in the IFU field is $2.9 \pm 2 \times 10^5 M_\odot$;

(viii) the estimated mass outflow rate along the east spiral arm is in the range $0.8 - 3.8 \times 10^{-2}\,M_\odot\,yr^{-1}$, which is somewhat higher than the mass accretion rate, $7.5 \times 10^{-3}\,M_\odot\,yr^{-1}$;

(ix) we estimate a low kinetic power for the outflow, in the range $0.8 - 6.2 \times 10^{38}$ ergs s^{-1}, representing $0.2 - 1.5 \times 10^{-3}\%$ of the bolometric luminosity.

On the basis of the above characteristics, we propose a scenario in which the gas observed in the inner kiloparsec of Arp 102B was captured in an interaction with its companion, Arp 102A and settled in a rotating disk in the inner kiloparsec. The inflow of this gas towards the nucleus ignited the nuclear activity, giving origin to a radio jet launched close to the plane of the sky. Interaction of the jet with the rotating gas gave origin to the arms which are regions of enhanced emission due to compression by the radio jet. The jet, launched approximately along the line of nodes of the rotating disk, gets deflected to high disk latitudes in a high density gas knot, dragging along gas located in the disk, forming the spiral arms. The enhanced emission in the arms can also be due to additional contribution from shock ionization by the radio jet.

Besides the outflow along the radio jet, we have also found another outflow, more compact – with the highest blueshifts observed at ≈ 300 pc to the south-east of the nucleus and a possible counterpart observed to the north-west. This seems to be a more recent outflow, oriented approximately perpendicular to the previous one.

Our observations do not give constraints to the mechanism responsible for the one-sidedness of the radio jet. We estimate that in order to distinguish possible mechanisms it is desirable to have more sensitive radio observations, possibly with JVLA. Higher resolution observations could add constraints to the younger perpendicular outflow.

REFERENCES

Allington-Smith, J. R., 2002, PASP, 114, 892
Baldwin, J.A., Phillips, M.M., Terlevich, R., 1981, PASP, 93, 5
Barbosa, F.K.B., Storchi-Bergmann, T., Cid Fernandes, R., Winge, C., Schmitt, H., 2006, MNRAS, 371, 170
Bertola, F., Bettoni, D., Danziger, J., Sadler, E., Sparke, L., de Zeeuw, T., 1991, ApJ, 373, 369
Biermann, P., Preuss, E., Kronberg, P.P., Schilizzi, R.T., Shaffer, D.B., 1981, ApJ, 250, 49
Caccianiga, A., March, M.J.M., Thean, A., Dennett-Thorpe, J., 2001, MNRAS, 328, 867
Cardelli, J.A., Clayton, G.C., & Mathis, J.S., 1989, ApJ, 345, 245
Cid Fernandes, R., Schoenell, W., Gomes, J.M., Asari, N.V., Schlickmann, M., Mateus, A., Stasinskas, G., Sodr, L., Jr., Torres-Papaqui, J.P., Seagal Collaboration, 2009, RMxAC, 35, 127
Chen, K., Halpern, J.P., & Filippenko, A.V., 1989, ApJ, 339, 742
Chen, K. & Halpern J.P., 1989, ApJ, 344, 115
Davies, R.I., Maciejewski, W., Hicks, E.K.S., Tacconi, L.J., Genzel, R., Engel, H., 2009, ApJ, 702, 114

de Vaucouleurs, G., de Vaucouleurs, A., Corwin, H.H., Buta, R.J., Paturel, G., Fouque, P., 1991, Third Reference Catalogue of Bright Galaxies (New York: Springer)
Eracleous, M. & Halpern, J. P., 2004, ApJS, 150, 181
Fathi, K., Storchi-Bergmann, T., Riffel, R.A., Winge, C., Axon, D.J., Robinson, A., Capetti, A., Marconi, A., 2006, ApJ, 641, L25
Fathi, K. Axon, D.J., Storchi-Bergmann, T., Kharb, P., Robinson, A., Marconi, A., Maciejewski, W., Capetti, A., 2011, ApJ, 736, 77
Frank, J., King, A., Raine, D.J., 2002, Accretion Power in Astrophysics, 3nd. ed., Cambridge Univ. Press, Cambridge
Flohic, H.M.L.G., & Eracleous, M., 2008, ApJS, 622, 178
Lucy, L.B., 1974, AJ, 79, 745
Kewley, L.J., Groves, B., Kauffmann, G., Heckman, T., 2006, MNRAS, 372, 961
Kharb, P., O'Dea, C.P., Baum, S.A., Colbert, E.J.M., Xu, C., 2006, ApJ, 652, 177
Maciejewski, W., 2004, MNRAS, 354, 892
Martini, P., Pogge, R.W., 1999, AJ, 118, 2646
Martini, P., Regan, M.W., Mulchaey, J.S., Pogge, R.W., 2003, ApjS, 146, 353
Newman, J.A., Eracleous, M., Filippenko, A.V., Halpern, J.P., 1997, ApJ, 485, 570
Osterbrock, D.E., Ferland, G.J., 1989, Astrophysics of Gaseous Nebulae and Active Galactic Nuclei, 2nd. ed., University Science Books, California
Peterson, B.M., 1997, An Introduction to Active Galactic Nuclei, Cambridge University Press, Cambridge
Prieto, M.A., Maciejewski, W., Reunanen, J., 2005, AJ, 130, 1472
Pogge, R.W., Martini, P., 2002, ApJ, 569, 624
Puschell, J.J., Moore, R., Cohen, R.D., Owen, F.N., Phillips, A.C., 1986, AJ, 91, 751
Richardson, W.H., 1972, JOSA, 62, 55
Riffel, R.A., Storchi-Bergmann, T., Winge, C., McGregor, P.J., Beck, T., Schmitt, H., 2008, MNRAS, 385, 1129
Riffel, R.A., Storchi-Bergmann, T., 2011, MNRAS, 417, 2752
Roy, A.L., Ulvestad, J.S., Wilson, A.S., Colbert, E.J.M., Mundell, C.G., Wrobel, J.M., Norris, R.P., Falcke, H., Krichbaum, T., 2000, in Perspectives on Radio Astronomy: Science with Large Antenna Arrays, ed. M. P. van Haarlem, 173
Schnorr Müller, A., Storchi-Bergmann, T., Riffel, R.A., Ferrari, F., Steiner, J.E., Axon, D.J., Robinson, A., 2011, MNRAS, 413, 149
Sikora, M., Stawarz, Ł.; Lasota, J.P., 2007, ApJ, 658, 815
Simões Lopes, R.D., Storchi-Bergmann, T., de Fatima Saraiva, M., Martini, P., 2007, ApJ, 655, 718
Stauffer, J., Schild, R., & Keel, W.C., 1983, ApJ, 270, 465
Steiner, J.E., Menezes, R.B., Ricci, T.V., Oliveira, A.S., 2009, MNRAS, 395, 64
Storchi-Bergmann, T., Baldwin, J. A., Wilson, A. S., 1993, ApJ, 410, L11
Storchi-Bergmann, T., et al., 2003, ApJ, 598, 956
Storchi-Bergmann, T., Dors, O. L., Riffel, R. A., 2007, ApJ, 670, 959
Storchi-Bergmann, T., Simões Lopes, R.D., McGregor, P.J., Riffel, R.A., Beck, T., Martini, P., 2010, MNRAS, 402, 819
van der Kruit, P.C., Allen, R.J., 1978, ARA&A, 16, 103
Wrobel, J.M., Harrison, B., Pedlar, A., Unger, S.W., 1988, MNRAS, 235, 663

Capítulo 3

Sumário e conclusões

Medimos a cinemática e excitação do gás nos kiloparsecs centrais da rádio-galáxia Arp 102B, classificada como LINER/Seyfert 1, usando espectros ópticos obtidos com o espectrógrafo de campo integral do instrumento GMOS no telescópio Gemini Norte. A motivação desse estudo era estudar a natureza dos braços espirais nucleares, sua relação com o jato rádio, e o papel desses componentes no cenário de *inflow* e *outflow* do núcleo ativo da galáxia.

Mapas de fluxo nas linhas de emissão mostram uma correlação entre o jato rádio e o braço espiral à leste. A emissão é mais intensa ao longo dos braços, principalmente a leste, sendo a oeste também evidente em [O III].

Baixa excitação do gás é encontrada ao longo dos braços, principalmente no braço à leste, com valores típicos de LINERs. Excitações do tipo LINER e Seyfert são vistas nos diagramas diagnósticos, fortalecendo a classificação anteriormente dada à atividade da Arp 102B. Nenhuma evidência de excitação típica de região HII foi encontrada. Isso indica que o gás ao longo dos braços não é ionizado por estrelas, favorecendo um cenário de ionização por choques ou então por um contínuo nuclear diluído.

Como era esperado, o maior avermelhamento é encontrado no núcleo. Os menores avermelhamentos são encontrados ao longo dos braços, sendo menor que o da região circundante. A densidade do gás é maior nos braços se comparada com outras regiões, exceto no núcleo, onde é máxima. Uma região de alta densidade à leste parece ser a origem da deflexão do jato rádio. Essa região também apresenta alto avermelhamento e baixa excitação, indicando a presença de gás denso e frio.

Mapas de velocidade centróide mostram um padrão de rotação distorcido, com *blueshifts* a leste e *redshifts* a oeste. O jato rádio se correlaciona com a região em *blueshift*, que apresenta velocidade menor do que a circundante. O fato da velocidade

ser menor nos leva à hipótese de que o jato sai do núcleo próximo ao plano do céu.

A dispersão de velocidades do gás é alta no núcleo e ao longo de uma região que vai de noroeste a sudeste – onde se observa uma região em *blueshift*. Ainda é razoavelmente grande ao longo dos braços, quando comparada a outras regiões. Isso indica que choques devem ser um mecanismo importante de excitação do gás ao longo dos braços.

Channel maps mostram o mesmo padrão de rotação. São observadas velocidades positivas e negativas ao longo do braço a leste (mesma região do jato rádio). Isso fortalece a interpretação de que o jato rádio está praticamente no plano do céu e somente levemente inclinado em nossa direção. O *outflow* seria aproximadamente cilíndrico, com o diâmetro do cilíndro aumentando à medida que aumenta a distância ao núcleo, mas como o centro do *outflow* está somente um pouco inclinado em nossa direção, vemos a parte da frente do *outflow* se aproximando e a parte de trás se afastando. Assim, favorecemos a interpretação de que o gás está em rotação, um pouco distorcida pelo *outflow* originado da interação do jato rádio com o gás circumnuclear.

Modelando a cinemática do gás, vemos que o mapa de velocidade centróide fica bem reproduzido por gás em rotação num disco com inclinação de $\approx 77°$ e linha dos nodos em PA $\approx 88°$ (se excluirmos a região em *blueshift* para sudeste). Um mapa de estrutura derivado da imagem (HST ACS) no contínuo, sugere que o lado próximo do disco em rotação é o norte. A alta inclinação do disco sugere que os braços espirais não pertencem ao mesmo.

A análise PCA feita no cubo de dados mostra que o jato rádio se correlaciona com a região que origina as linhas estreitas de emissão. Ainda é possível ver uma componente em *outflow* perpendicular ao jato rádio, que interpretamos ser correspondente à região em *blueshift* observada no mapa de velocidade centróide, onde também observamos um valor alto da dispersão de velocidades.

Aproximando a geometria do *outflow* co-espacial ao jato rádio por um cilindro, medimos uma taxa de *outflow* de $0.78 - 3.77 \times 10^{-2}\,\mathrm{M_\odot\,yr^{-1}}$, não muito maior que o valor encontrado para taxa de acreção de $7.51 \times 10^{-3}\,\mathrm{M_\odot\,yr^{-1}}$. Além disso foi estimada uma massa de gás emissora de $2.89 \pm 2.04 \times 10^5 M_\odot$, e uma potência do jato pequena, apenas $0.78 - 6.19 \times 10^{38}\,\mathrm{ergs\,s^{-1}}$, o que corresponde a $0.2 - 1.5 \times 10^{-3}\%$ da luminosidade bolométrica.

O cenário que propomos para o gás, braços espirais e jato rádio em Arp 102B é o seguinte: o gás observado nos kiloparsecs centrais da galáxia Arp 102B foi capturado em uma interação com sua companheira, Arp 102A, e criou o que parece

ser um disco em rotação. A atividade deve ter sido iniciada com a queda do gás no potencial gravitacional do núcleo, originando então o jato rádio, que é lançado próximo ao plano do céu. Esse jato entra em interação com o gás em rotação, gerando a emissão vista em forma de braços espirais, devido a compressão do gás pelo jato. O jato parece ser então desviado por uma região de alta densidade $\approx 1\,\mathrm{kpc}$ a leste do núcleo. Além disso, existem evidências de um segundo outflow provavelmente mais jovem e perpendicular ao primeiro.

3.1 Perspectivas

Uma característica do espectro de Arp 102B que não destacamos no trabalho foi a sua emissão em duplo-pico observada nas linhas de Balmer. Esta emissão é característica de um disco de acreção, que, por sua vez é também origem (embora nas suas partes centrais) do jato rádio. Já possuímos dados espectroscópicos de campo integral de outras duas galáxias que também têm jatos rádio e emissão em duplo-pico: Pictor A e 3C 234. Uma curiosidade é que 3C 234 apresenta também braços espirais nucleares.

Como próximo passo pretendemos fazer um estudo semelhante ao feito em Arp 102B nestes dois obejtos, investigando possíveis características comuns e a relação entre o jato rádio e o gás emissor.

Bibliografia

[1] ALLINGTON-SMITH, J., MURRAY, G., CONTENT, R., DODSWORTH, G., DAVIES, R., MILLER, B. W., JORGENSEN, I., HOOK, I., CRAMPTON, D., MUROWINSKI, R. Integral Field Spectroscopy with the Gemini Multiobject Spectrograph. I. Design, Construction, and Testing. , v. 114, p. 892–912, August 2002.

[2] ANTONUCCI, R. Unified models for active galactic nuclei and quasars. , v. 31, p. 473–521, 1993.

[3] ANTONUCCI, R. Thermal and Nonthermal Radio Galaxies. **ArXiv e-prints**, January 2011.

[4] BALDWIN, J. A., PHILLIPS, M. M., TERLEVICH, R. Classification parameters for the emission-line spectra of extragalactic objects. , v. 93, p. 5–19, February 1981.

[5] BIERMANN, P., PREUSS, E., KRONBERG, P. P., SCHILIZZI, R. T., SHAFFER, D. B. VLBI and X-ray observations of compact nuclei in pairs of galaxies. , v. 250, p. L49–L53, November 1981.

[6] CACCIANIGA, A., MARCHÃ, M. J. M., THEAN, A., DENNETT-THORPE, J. EVN observations of low-luminosity flat-spectrum active galactic nuclei. , v. 328, p. 867–872, December 2001.

[7] CARDELLI, J. A., CLAYTON, G. C., MATHIS, J. S. The relationship between infrared, optical, and ultraviolet extinction. , v. 345, p. 245–256, October 1989.

[8] CHEN, K., HALPERN, J. P. Structure of line-emitting accretion disks in active galactic nuclei - ARP 102B. , v. 344, p. 115–124, September 1989.

[9] CHEN, K., HALPERN, J. P., FILIPPENKO, A. V. Kinematic evidence for a relativistic Keplerian disk - ARP 102B. , v. 339, p. 742–751, April 1989.

[10] DAVIES, R. I., MACIEJEWSKI, W., HICKS, E. K. S., TACCONI, L. J., GENZEL, R., ENGEL, H. Stellar and Molecular Gas Kinematics Of NGC 1097: Inflow Driven by a Nuclear Spiral. , v. 702, p. 114–128, September 2009.

[11] ELITZUR, M. The obscuring *torus* in AGN. , v. 50, p. 728–731, November 2006.

[12] ERACLEOUS, M., HALPERN, J. P. Accurate Redshifts and Classifications for 110 Radio-Loud Active Galactic Nuclei. , v. 150, p. 181–186, January 2004.

[13] FANAROFF, B. L., RILEY, J. M. The morphology of extragalactic radio sources of high and low luminosity. , v. 167, p. 31P–36P, May 1974.

[14] FATHI, K., AXON, D. J., STORCHI-BERGMANN, T., KHARB, P., ROBINSON, A., MARCONI, A., MACIEJEWSKI, W., CAPETTI, A. An Hα Nuclear Spiral Structure in the E0 Active Galaxy Arp 102B. , v. 736, p. 77, August 2011.

[15] FATHI, K., STORCHI-BERGMANN, T., RIFFEL, R. A., WINGE, C., AXON, D. J., ROBINSON, A., CAPETTI, A., MARCONI, A. Streaming Motions toward the Supermassive Black Hole in NGC 1097. , v. 641, p. L25–L28, April 2006.

[16] FERRARESE, L., FORD, H. Supermassive Black Holes in Galactic Nuclei: Past, Present and Future Research. , v. 116, p. 523–624, February 2005.

[17] FERRARESE, L., MERRITT, D. A Fundamental Relation between Supermassive Black Holes and Their Host Galaxies. , v. 539, p. L9–L12, August 2000.

[18] GEBHARDT, K., BENDER, R., BOWER, G., DRESSLER, A., FABER, S. M., FILIPPENKO, A. V., GREEN, R., GRILLMAIR, C., HO, L. C., KORMENDY, J., LAUER, T. R., MAGORRIAN, J., PINKNEY, J., RICHSTONE, D., TREMAINE, S. A Relationship between Nuclear Black Hole Mass and Galaxy Velocity Dispersion. , v. 539, p. L13–L16, August 2000.

[19] HECKMAN, T. M. An optical and radio survey of the nuclei of bright galaxies - Activity in normal galactic nuclei. , v. 87, p. 152–164, July 1980.

[20] KEWLEY, L. J., GROVES, B., KAUFFMANN, G., HECKMAN, T. The host galaxies and classification of active galactic nuclei. , v. 372, p. 961–976, November 2006.

[21] KOVALEV, Y. Y., LISTER, M. L., HOMAN, D. C., KELLERMANN, K. I. The Inner Jet of the Radio Galaxy M87. , v. 668, p. L27–L30, October 2007.

[22] LUCY, L. B. An iterative technique for the rectification of observed distributions. , v. 79, p. 745, June 1974.

[23] MACIEJEWSKI, W. Nuclear spirals in galaxies: gas response to an asymmetric potential - II. Hydrodynamical models. , v. 354, p. 892–904, November 2004.

[24] MARTINI, P., POGGE, R. W. Hubble Space Telescope Observations of the CFA Seyfert 2 Galaxies: The Fueling of Active Galactic Nuclei. , v. 118, p. 2646–2657, December 1999.

[25] MARTINI, P., REGAN, M. W., MULCHAEY, J. S., POGGE, R. W. Circumnuclear Dust in Nearby Active and Inactive Galaxies. II. Bars, Nuclear Spirals, and the Fueling of Active Galactic Nuclei. , v. 589, p. 774–782, June 2003.

[26] MCCONNELL, N. J., MA, C.-P., GEBHARDT, K., WRIGHT, S. A., MURPHY, J. D., LAUER, T. R., GRAHAM, J. R., RICHSTONE, D. O. Two ten-billion-solar-mass black holes at the centres of giant elliptical galaxies. , v. 480, p. 215–218, December 2011.

[27] MORGAN, C. W., KOCHANEK, C. S., MORGAN, N. D., FALCO, E. E. The Quasar Accretion Disk Size-Black Hole Mass Relation. , v. 712, p. 1129–1136, April 2010.

[28] OKE, J. B. Emission-line profile changes in 3C 390.3. In: SUPERLUMINAL RADIO SOURCES, Zensus, J. A., Pearson, T. J., editores, p. 267–272, 1987.

[29] OSTERBROCK, D. E. **Astrophysics of gaseous nebulae and active galactic nuclei**: 1989.

[30] PEREZ, E., MEDIAVILLA, E., PENSTON, M. V., TADHUNTER, C., MOLES, M. An accretion disc in the broad-line radio galaxy 3C 390.3? , v. 230, p. 353–362, February 1988.

[31] PETERSON, B. M. **An Introduction to Active Galactic Nuclei**: February 1997.

[32] PETERSON, B. M., FERRARESE, L., GILBERT, K. M., KASPI, S., MALKAN, M. A., MAOZ, D., MERRITT, D., NETZER, H., ONKEN, C. A., POGGE, R. W., VESTERGAARD, M., WANDEL, A. Central Masses and Broad-Line Region Sizes of Active Galactic Nuclei. II. A Homogeneous Analysis of a Large Reverberation-Mapping Database. , v. 613, p. 682–699, October 2004.

[33] PRIETO, M. A., MACIEJEWSKI, W., REUNANEN, J. Feeding the Monster: The Nucleus of NGC 1097 at Subarcsecond Scales in the Infrared with the Very Large Telescope. , v. 130, p. 1472–1481, October 2005.

[34] PUSCHELL, J. J., MOORE, R., COHEN, R. D., OWEN, F. N., PHILLIPS, A. C. Observations of the low-luminosity broad-line radio galaxy 1717 + 49. , v. 91, p. 751–754, April 1986.

[35] RICHARDSON, W. H. Bayesian-Based Iterative Method of Image Restoration. **Journal of the Optical Society of America (1917-1983)**, v. 62, p. 55, January 1972.

[36] RIFFEL, R. A. profit: a new alternative for emission-line profile fitting. , v. 327, p. 239–244, June 2010.

[37] RIFFEL, R. A., STORCHI-BERGMANN, T., NAGAR, N. M. Near-infrared dust and line emission from the central region of Mrk1066: constraints from Gemini NIFS. , v. 404, p. 166–179, May 2010.

[38] RIFFEL, R. A., STORCHI-BERGMANN, T., WINGE, C., MCGREGOR, P. J., BECK, T., SCHMITT, H. Mapping of molecular gas inflow towards the Seyfert nucleus of NGC4051 using Gemini NIFS. , v. 385, p. 1129–1142, April 2008.

[39] SCHNORR MÜLLER, A., STORCHI-BERGMANN, T., RIFFEL, R. A., FERRARI, F., STEINER, J. E., AXON, D. J., ROBINSON, A. Gas streaming motions towards the nucleus of M81. , v. 413, p. 149–161, May 2011.

[40] SIMÕES LOPES, R. D., STORCHI-BERGMANN, T., DE FÁTIMA SARAIVA, M., MARTINI, P. A Strong Correlation between Circumnuclear Dust and Black Hole Accretion in Early-Type Galaxies. , v. 655, p. 718–734, February 2007.

[41] STASIŃSKA, G., VALE ASARI, N., CID FERNANDES, R., CID FERNANDES, . Beware of Fake AGNs. In: IAU SYMPOSIUM, v. 267 of **IAU Symposium**, p. 141–141, May 2010.

[42] STAUFFER, J., SCHILD, R., KEEL, W. ARP 102B - A new and unusual broad-line galaxy. , v. 270, p. 465–470, July 1983.

[43] STEINER, J. E., MENEZES, R. B., RICCI, T. V., OLIVEIRA, A. S. PCA Tomography: how to extract information from data cubes. , v. 395, p. 64–75, May 2009.

[44] STORCHI-BERGMANN, T., BALDWIN, J. A., WILSON, A. S. Double-peaked broad line emission from the LINER nucleus of NGC 1097. , v. 410, p. L11–L14, June 1993.

[45] STORCHI-BERGMANN, T., DORS, O. L., JR., RIFFEL, R. A., FATHI, K., AXON, D. J., ROBINSON, A., MARCONI, A., ÖSTLIN, G. Nuclear Spirals as Feeding Channels to the Supermassive Black Hole: The Case of the Galaxy NGC 6951. , v. 670, p. 959–967, December 2007.

[46] STORCHI-BERGMANN, T., NEMMEN DA SILVA, R., ERACLEOUS, M., HALPERN, J. P., WILSON, A. S., FILIPPENKO, A. V., RUIZ, M. T., SMITH, R. C., NAGAR, N. M. Evolution of the Nuclear Accretion Disk Emission in NGC 1097: Getting Closer to the Black Hole. , v. 598, p. 956–968, December 2003.

[47] URRY, C. M., PADOVANI, P. Unified Schemes for Radio-Loud Active Galactic Nuclei. , v. 107, p. 803, September 1995.

[48] WROBEL, J. M., HARRISON, B., PEDLAR, A., UNGER, S. W. A one-sided radio jet in the elliptical galaxy NGC 6146. , v. 235, p. 663–671, December 1988.